Economic Geology, v. 118, no. 6, pp. 1341–1370

The Age and Origin of the Ruwai Polymetallic Skarn Deposit, Indonesia: Evidence of Cretaceous Mineralization in the Central Borneo Metallogenic Belt

Cendi D.P. Dana,[1,2,†] Andrea Agangi,[2] Arifudin Idrus,[3] Cyril Chelle-Michou,[4] Chun-Kit Lai,[5,6] Mizuki Ishida,[7] Marcel Guillong,[4] Ignacio González-Álvarez,[8,9] Ryohei Takahashi,[2] Moei Yano,[10,11] Kazuhide Mimura,[10,11] Junichiro Ohta,[10,11] Yasuhiro Kato,[7,10] Doly R. Simbolon,[12] and Xiao-Ping Xia[13]

[1]*School of GeoSciences, Grant Institute, The University of Edinburgh, Edinburgh EH9 3FE, United Kingdom*

[2]*Graduate School of International Resource Sciences, Akita University, Akita 010-0852, Japan*

[3]*Department of Geological Engineering, Universitas Gadjah Mada, Yogyakarta 55281, Indonesia*

[4]*Department of Earth Sciences, ETH Zurich, Zurich 8092, Switzerland*

[5]*Global Project Generation and Targeting, Fortescue Metals Group Ltd., East Perth, Western Australia 6004, Australia*

[6]*Faculty of Science, Universiti Brunei Darussalam, BE 1410 Gadong, Brunei Darussalam*

[7]*Department of Systems Innovation, School of Engineering, The University of Tokyo, Tokyo 113-8656, Japan*

[8]*Commonwealth Scientific and Industrial Research Organisation (CSIRO), Mineral Resources, Discovery Program, Perth, Western Australia 6151, Australia*

[9]*University of Western Australia, Centre for Exploration Targeting, Perth, Western Australia 6009, Australia*

[10]*Ocean Resources Research Center for Next Generation, Chiba Institute of Technology, Chiba 275-0016, Japan*

[11]*Frontier Research Center for Energy and Resources, School of Engineering, The University of Tokyo, Tokyo 113-8656, Japan*

[12]*PT Kapuas Prima Coal, Tbk., North Jakarta 14460, Indonesia*

[13]*State Key Laboratory of Isotope Geochemistry, Guangzhou Institute of Geochemistry, Chinese Academy of Sciences, Guangzhou, China*

Abstract

The Ruwai skarn deposit is the largest polymetallic skarn deposit in Borneo and is located in the Schwaner Mountains. The skarns and massive orebodies are hosted in marble of the Jurassic Ketapang Complex, which was intruded by Cretaceous Sukadana granitoids. The prograde-stage garnet and retrograde-stage titanite yielded U-Pb ages of 97.0 ± 1.8 to 94.2 ± 10.3 Ma and 96.0 ± 2.9 to 95.0 ± 2.0 Ma, respectively. These ages are similar to Re-Os ages obtained on sulfides (96.0 ± 2.3 Ma) and magnetite (99.3 ± 3.6 Ma). The U-Pb zircon ages reveal that magmatism at Ruwai occurred in three phases, including the Early Cretaceous (ca. 145.7 and 106.7–105.7 Ma; andesite-dacite), Late Cretaceous (ca. 99.7–97.1 Ma; diorite-granodiorite), and late Miocene (ca. 10.94–9.51 Ma; diorite-dolerite). Based on geochemical and stable isotopic data (C-O-S) the Ruwai skarn ores are interpreted to have formed from oxidized fluids at ca. 160 to 670°C. The ore-forming fluids and metals were mostly magmatic in origin but with significant crustal input. Ruwai skarn mineralization occurred in the Late Cretaceous, associated with Paleo-Pacific subduction beneath Sundaland after the Southwest Borneo accretion. Ruwai is the first occurrence of Cretaceous mineralization recognized in the Central Borneo metallogenic belt.

Introduction

The island of Borneo has a significant proven metal endowment (e.g., Harahap et al., 2013; van Leeuwen, 2018), as well as largely underexplored regions covered by extensive tropical rainforest and swamp. Borneo hosts a number of important ore deposits along the Central Borneo metallogenic belt, including the giant Kelian epithermal Au deposit and the significant ore fields of Bau (epithermal/sediment-hosted Au), Buduk (Cu-Au skarn), Ruwai (Fe-Zn-Pb-Ag ± Cu skarn), Mt. Muro (epithermal Au-Ag), Seruyung (epithermal Au), and Mamut (porphyry Cu-Au) (Fig. 1e; Harahap et al., 2013; van Leeuwen, 2018). Among these, the Buduk Cu-Au and Ruwai Fe-Zn-Pb-Ag deposits are the only economically viable skarns. The discovery of the Ruwai skarn deposit dates back to 1918 by a Dutch investigation program, which was followed by Renison Goldfields Consolidated Ltd. (1987–1991), PT Tebolai Seng Perdana (1992–1996), and Scorpion Schwaner Mineral, Inc. (1996–1997). Since 2005, the Ruwai skarn deposit has been mined for Fe-Zn-Pb-Ag by PT Kapuas Prima Coal, Tbk. A recent estimation by Mining One Pty Ltd. indicates a total resource of 14.43 Mt at 4.94% Zn, 3.28% Pb, and 108.11 g/t Ag (S. Hutchin, unpub. report, 2018), making it one of the largest Pb-Zn skarn deposits in Indonesia. Despite its large resource and long history of exploration, studies of the geochronology and geochemical characteristics of this deposit are lacking.

The identification of the intrusions responsible for skarn mineralization in Borneo remains speculative; there are two

[†]Corresponding author: e-mail, c.d.p.dana@sms.ed.ac.uk

ISSN 0361-0128; doi:10.5382/econgeo.5009; 30 p.
Digital appendices are available in the online Supplements section.

Submitted: August 1, 2022/Accepted: January 30, 2023

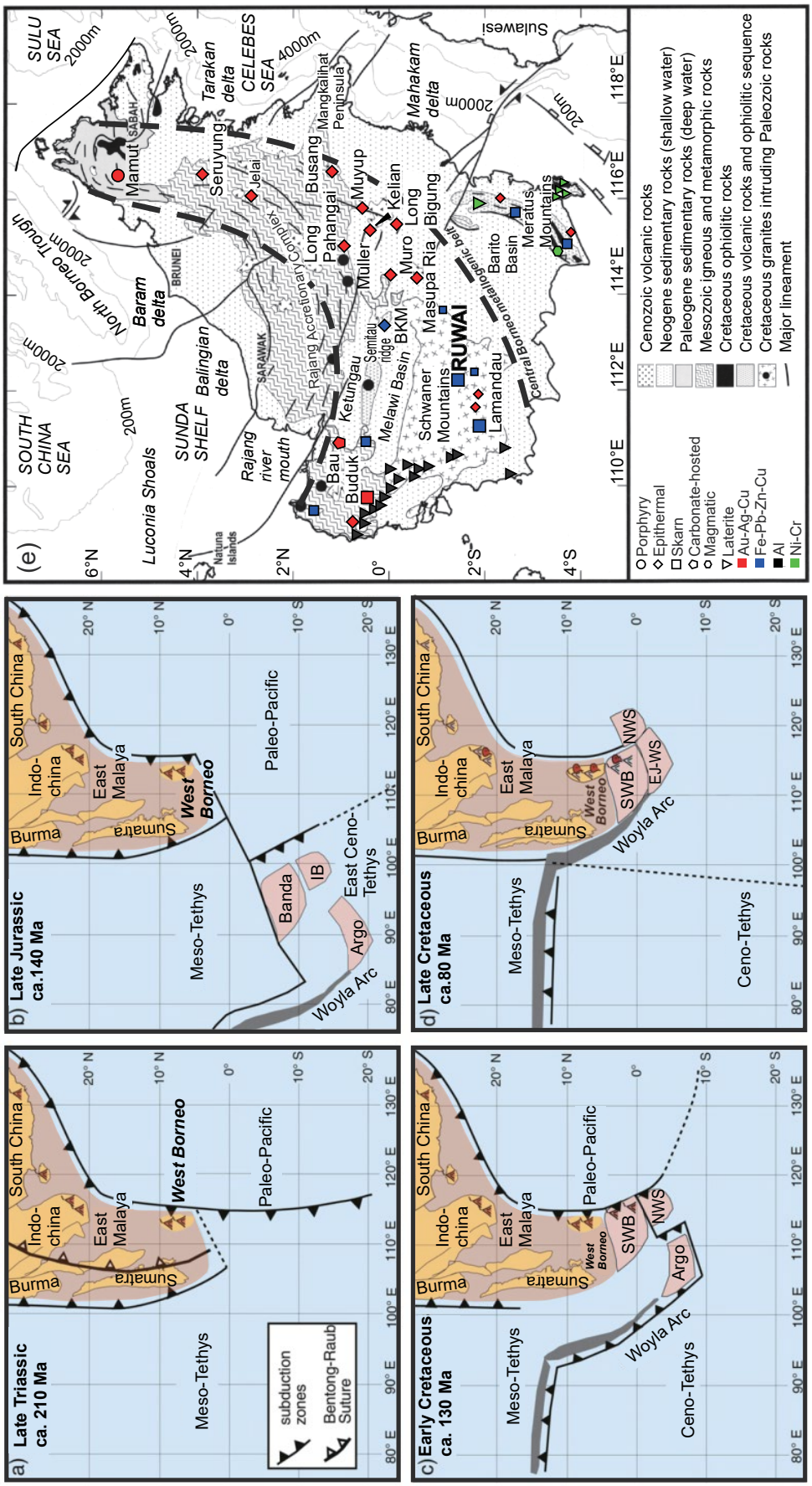

Fig. 1. (a-d) Mesozoic tectono-magmatic evolution at the Paleo-Pacific subduction zone (modified after Hennig et al., 2017). (e) Regional physiography and geologic framework of Borneo Island. The Ruwai skarn deposit is located within the Schwaner Mountains complex in the southwestern part of the island (modified after Hall and Nichols, 2002). Abbreviations: IB = Inner Banda, EJ-WS = East Java-West Sulawesi, NWS = Northwest Sulawesi, SWB = Southwest Borneo.

possible candidates: (1) Oligo-Miocene intrusions associated with the Sintang Suite (e.g., Gunter, 2011) and (2) Cretaceous intrusions associated with the Sukadana granitoid (e.g., D. Cooke and P. Kitto, unpub. report, 1997). Although some previous studies suggested that the Cretaceous Sukadana granitoid is synmineralization (e.g., Idrus et al., 2011; Setijadji et al., 2011; Simbolon et al., 2019), this has not been confirmed previously by direct geochronological results.

In this study, we present new zircon U-Pb-Hf isotope and whole-rock geochemical data of the multiphase volcanic and plutonic rocks at Ruwai, U-Pb analyses of garnet and titanite, and Re-Os analyses of sulfides and magnetite. These data constrain the mineralization age and identify the causative intrusion(s) associated with skarn mineralization at Ruwai. In addition, we present elemental and isotopic data to constrain the genesis of Ruwai and evaluate the implications for exploration in the Central Borneo metallogenic belt.

Geologic Background

Tectono-metallogeny of Borneo

The Paleozoic-Mesozoic basement in Borneo is unconformably overlain by a Cenozoic sedimentary basin (Hall and Nichols, 2002; Breitfeld et al., 2017; Fig. 1e). During the Paleozoic, Borneo was possibly still part of the Gondwana supercontinent (e.g., van Bemmelen, 1949; Metcalfe, 2013). The oldest Paleozoic unit recorded in Borneo is a schist from the Embuoi Complex in the northwest of the island, which yielded zircon U-Pb ages of 462.4 ± 2.6 to 453.3 ± 1.9 Ma (Zhu et al., 2022). Borneo then experienced prolonged tectonic events and related magmatic activity throughout the Mesozoic, the products of which are mostly preserved in the Schwaner Mountains. During the Triassic, arc-related magmatic activity resulted from the subduction of the Paleo-Pacific plate under the eastern Sundaland margin (Breitfeld et al., 2017; Hennig et al., 2017; Fig. 1a). Multiple Triassic magmatic events are represented by various formations, including the granitoids of the Embuoi Complex (K-Ar ages ca. 320 ± 3–201 ± 2 Ma; Williams et al., 1988), Jagoi granodiorite (U-Pb ages ca. 217 ± 1–208 ± 1 Ma; Breitfeld et al., 2017) and metatonalite in the northwestern Schwaner Mountains (U-Pb age 233 ± 3 Ma; Setiawan et al., 2013). Jurassic magmatism only occurred in the southern Schwaner Mountains (i.e., Belaban granite, ca. 186.7 ± 2.3–153.5 ± 3.5 Ma; Mentembah granite, 151.2 ± 1.2 Ma) as a consequence of the continuing Paleo-Pacific subduction during separation of the Southwest Borneo block from Gondwana (Davies et al., 2014; Hennig et al., 2017; Breitfeld et al., 2020). The Middle-Late Jurassic was characterized by the formation of a carbonate platform, the Ketapang Complex, which rapidly subsided during the Early Cretaceous (Morley, 1998; Basir and Uyop, 1999; Hennig et al., 2017). This complex consists of fossiliferous limestone in its lower part and clastic units (including siltstone-sandstone, crystal-lithic tuff, and graphite-bearing shale) in its upper part (Simbolon et al., 2019, and references therein). Limited palynologic analyses on the Ketapang Complex yielded Jurassic and Cretaceous (Albian-Cenomanian) ages (Haile, 1973; De Keyser and Rustandi, 1993), whereas recent U-Pb detrital zircon dating from the sandstone unit suggested that the maximum depositional age is Late Cretaceous (Campanian), around 78.0 ± 0.8 Ma (Li et al., 2021). No pre-Cretaceous-age mineral deposits have been documented within the Central Borneo metallogenic belt, although Coggon et al. (2010) reported that platinum group mineralization in Meratus Mountains, an accretionary complex in easternmost Borneo, has an Early Jurassic age based on Pt-Os dating (197.8 ± 8.1 Ma).

The Cretaceous was the most active magmatic period in the region, producing granitoids that crop out in the northern and southern Schwaner Mountains (e.g., Sepauk tonalite, ca. 118.6 ± 1.1–111.8 ± 1.1 Ma; Laur granite, ca. 101.5 ± 0.6–96.8 ± 0.6 Ma; Sukadana granite, ca. 84.7 ± 1.3–78.4 ± 0.5 Ma; Bretifeld et al., 2020), some of which have been metamorphosed (i.e., Pinoh Metamorphic Group, ca. 131.3 ± 1.0–110.1 ± 0.7 Ma; Bretifeld et al., 2020). This magmatic activity resulted from subduction of the Paleo-Pacific margin immediately after the accretion of the Southwest Borneo block to Sundaland in the Early Cretaceous (Hall, 2012; Breitfeld et al., 2017; Hennig et al., 2017). Late Cretaceous postcollisional magmatism followed the collision between the East Java and West Sulawesi blocks and ended the Mesozoic magmatic cycle (Davies et al., 2014; Hennig et al., 2017). Currently only one mineral deposit in the Central Borneo metallogenic belt, the Lamandau Fe-Cu deposit, is reported to have a Cretaceous age (U-Pb zircon ages of intrusions ca. 82.1 ± 1.7–78.7 ± 2.3 Ma; Li et al., 2015), although this age has not been confirmed by direct dating of the mineralization.

Tectonic activity during the Cenozoic was accompanied by subduction-related volcanism and basin formation, which was mainly controlled by the 35° counterclockwise rotation of Borneo (e.g., Hall and Nichols, 2002; Hall, 2012; Advokaat et al., 2018). Previous studies suggested that the Borneo block became a part of Sundaland during the middle Eocene (Hall et al., 2008; Advokaat et al., 2018). Paleogene magmatism, which started during the Eocene, was characterized by subduction-related calc-alkaline volcanism associated with the formation of the South China Sea and SE-directed subduction in the Rajang accretionary complex (Soeria-Atmadja et al., 1999; Fig. 1). Currently only two epithermal gold prospects, Long Bigung (K-Ar age: 40.6 ± 4.4 Ma) and Long Pahagai (K-Ar age: 48.6 ± 1.0 Ma), are known to be associated with Eocene magmatism (Baharuddin, 2011). Neogene magmatism, while still associated with subduction, changed from high-K calc-alkaline during the Mio-Pliocene, to tholeiitic Plio-Pleistocene within-plate basalt (Soeria-Atmadja et al., 1999). Among the Neogene magmatism products, the Sintang Suite has an important role, as most epithermal gold deposits in the Central Borneo metallogenic belt have close spatial and temporal associations with this suite (e.g., Muyup, Masuparia, Kelian, etc.; Thompson et al., 1994; Davies et al., 2008; Baharuddin, 2011). The Sintang Suite was dated by K-Ar at ca. 30.4 ± 0.9 to 23.0 ± 0.7 Ma (Melawi basin) and 17.9 ± 0.2 to 16.4 ± 0.1 Ma (Ketungau basin) in Northwest Kalimantan (Williams and Harahap, 1987) and more recently by U-Pb to ca. 21.1 ± 0.2 to 18.6 ± 0.2 Ma in West Sarawak (Breitfeld et al., 2019). Comprehensive geochronological study on the Kelian deposit demonstrated that the epithermal gold mineralization (K-Ar ages on sericite: 20.8 ± 0.5–20.6 ± 0.2 Ma; adularia: 20.2 ± 0.3 Ma; van Leuween et al., 1990; Abidin, 1996) has a close relationship with emplacement of the Sintang Suite (U-Pb ages of andesite: 19.70 ± 0.06 Ma; quartz-phyric rhyolite: 19.8 ± 0.1 Ma;

quartz-feldspar-phyric rhyolite: 19.5 ± 0.1 Ma; Setiabudi, 2001; Davies, 2002; Davies et al., 2008). The Mamut porphyry Cu-Au deposit (K-Ar age: 6.98 ± 0.30 Ma) is the youngest known mineral deposit found in Borneo (Imai, 2000).

Geology of the Ruwai skarn deposit

The oldest formation found at Ruwai belongs to the Matan Complex (also known as Kuayan Formation; Hermanto et al., 1994), which is attributed to be Upper Triassic-Middle Cretaceous and comprises mainly hornfelsed felsic volcanic rocks (including crystal-lithic tuff) and siltstone interbeds. The Matan Complex crops out mainly in the Southwest Gossan and Karim zones, where it was intruded by the Sukadana granite and then by the Sintang intermediate-mafic intrusions (J.M.R. Ayson, unpub. report, 1997; D. Cooke and P. Kitto, unpub. report, 1997; Idrus et al., 2011; Dana et al., 2019; Simbolon et al., 2019; Widyastanto et al., 2019). Most of the sedimentary units at Ruwai belong to the Jurassic Ketapang Complex, which is the most common and thickest unit in the Ruwai area. It can be generally subdivided into two main packages, with pelitic rocks overlain by carbonate units. The pelitic unit consists of siltstone, sandstone, and carbonaceous shale, while the carbonate unit consists of limestone and marl (Dana et al., 2019; Simbolon et al., 2019). In the Ruwai area, these lithologies have undergone contact metamorphism during granitoid emplacement, resulting in hornfels and marble. The Ketapang Complex is unconformably overlain by the Cretaceous bimodal Kerabai Volcanics (K-Ar age: 74.8 ± 0.7–65.6 ± 1.1 Ma; De Keyser and Rustandi, 1993; Fig. 2c). Mineralogical and geochemical evidence shows that these intrusions are classified as I-type and magnetite-series granitoids (Widyastanto et al., 2019; Dana et al., 2022a). The main intrusions, mostly found in the Gojo and Southwest Gossan zones, consist of granodiorite, monzonite, and quartz diorite. The more mafic intrusions include several types of diorite (quartz diorite, diorite, diorite porphyry, and microdiorite) and dolerite. Apart from dolerite dikes and younger diorite that intruded all other lithological units/suites, including the orebodies, there is no field evidence of crosscutting relationships between the quartz diorite, monzonite, or granodiorite.

The Ruwai skarn deposit consists of four mineralized zones (Fig. 2): (1) Gojo, (2) Karim, (3) Central Gossan, and (4) Southwest Gossan. Based on their mineralogy and metal zoning, Gojo-Karim can be considered as the proximal zone, while Central Gossan and Southwest Gossan are the distal zones (J.M.R. Ayson, unpub. report, 1997; D. Cooke and P. Kitto, unpub. report, 1997; Simbolon et al., 2019). These zones are distributed along a NE-SW–trending thrust fault, which acted as the main structural control for mineralization (Idrus et al., 2011; Setijadji et al., 2011; Simbolon et al., 2019). In the Central Gossan zone, the thrust fault is manifested as a mineralized fault breccia. Near-surface exposures of each orebody have mostly been affected by supergene argillic alteration, which caused pervasive replacement by swelling clays and moderate-intense oxidation. Below the weathered part, chlorite-calcite-epidote (propylitic alteration) is common, and secondary K-feldspar and biotite (potassic alteration) has altered the volcanic rocks locally.

The prograde skarn mineral assemblage at Ruwai is dominated by garnet, diopside, and wollastonite (Fig. 3). Accessory minerals include the rare earth element (REE)- and high field strength element (HFSE)-bearing minerals, zircon, thorite, monazite, and cerite (App. Fig. A1). These typically fine grained (0.5–20 μm) phases have euhedral (prismatic) shapes and can be found either as inclusions of single crystals or clusters within garnet. Retrograde phase minerals consist of epidote, amphibole, and phyllosilicate group minerals (Fig. 4). Epidote group minerals, the most common retrograde phases, consist of epidote sensu stricto and allanite. Other abundant retrograde minerals include phyllosilicates, among which the most abundant is chlorite, in addition to corrensite (interstratified chlorite and smectite), stilpnomelane, and illite. In the amphibole group minerals, ferroactionolite and manganese actinolite are most common. Calcite, quartz, titanite, rutile, and apatite are other retrograde phases, with some calcite, quartz, and apatite also associated with the prograde phase. Retrograde titanite and rutile are typically associated with epidote.

At Ruwai, the orebodies can be subdivided into three main groups based on mineralogical assemblages, including massive magnetite, massive sulfides, and massive pyrrhotite (Fig. 5). Magnetite mineralization is commonly found in Gojo-Karim and is mostly associated with garnet skarn. The magnetite bodies vary in thickness (1–15 m), with grades up to 1.0 m at 53.8% Fe and 0.02% Cu (PT Kapuas Prima Coal, Tbk., unpub. data, 2020). Massive sulfide mineralization extends from the western part of Karim to the southwestern part of the Southwest Gossan zones. It is characterized by sphalerite and galena and minor amounts of pyrrhotite and pyrite and is the main source of Zn-Pb-Ag ore, with average grades of 14.6% Zn, 6.4% Pb, 0.5% Cu, and 360.8 g/t Ag in 1.0 m of massive sulfide (PT Kapuas Prima Coal, Tbk., unpub. data, 2020). The last type of mineralization, massive pyrrhotite, is only found in the Central Gossan and Southwest Gossan zones. It is characterized by abundant pyrrhotite with fine-grained disseminated sphalerite and trace amounts of chalcopyrite. The average grades are typically 0.05% Pb, 5% Zn, and 15 g/t Ag in 1.0 m, and it is a secondary lead-zinc source (Simbolon et al., 2019).

In Ruwai, the ore minerals generally can be divided into four groups: (1) sulfides, (2) oxides, (3) arsenides, and (4) Bi-Ag bearing minerals. The sulfide group consists of pyrite, sphalerite, galena, pyrrhotite, chalcopyrite, and marcasite (Fig. 6). Pyrite has commonly been partially to completely replaced by galena, pyrrhotite, or magnetite. Pyrrhotite and chalcopyrite commonly occur as exsolution phases within sphalerite. The oxide group consists of magnetite, hematite, and ilmenite. Hematite has typically replaced magnetite (Fig. 6b), and both are mostly found in massive magnetite bodies, although some minor disseminated magnetite occurs in the surrounding wall rocks. In contrast, ilmenite was only identified in trace amounts in massive pyrrhotite. The arsenide group consists of arsenopyrite, cobaltite, and glaucodot. Minor arsenopyrite occurs in association with other sulfides. Cobaltite and glaucodot typically occur in solid solution with arsenopyrite. The Bi-Ag–bearing minerals consist of at least nine different species including tetrahedrite, native bismuth, cosalite, tsumoite, bismuthinite, joseite, Bi-Te-S, Bi-Te-Ag, and Bi-Ag-S (Dana et al., 2022b). The Bi-bearing minerals typically occur as inclusions in galena or pyrite, although fine disseminated grains

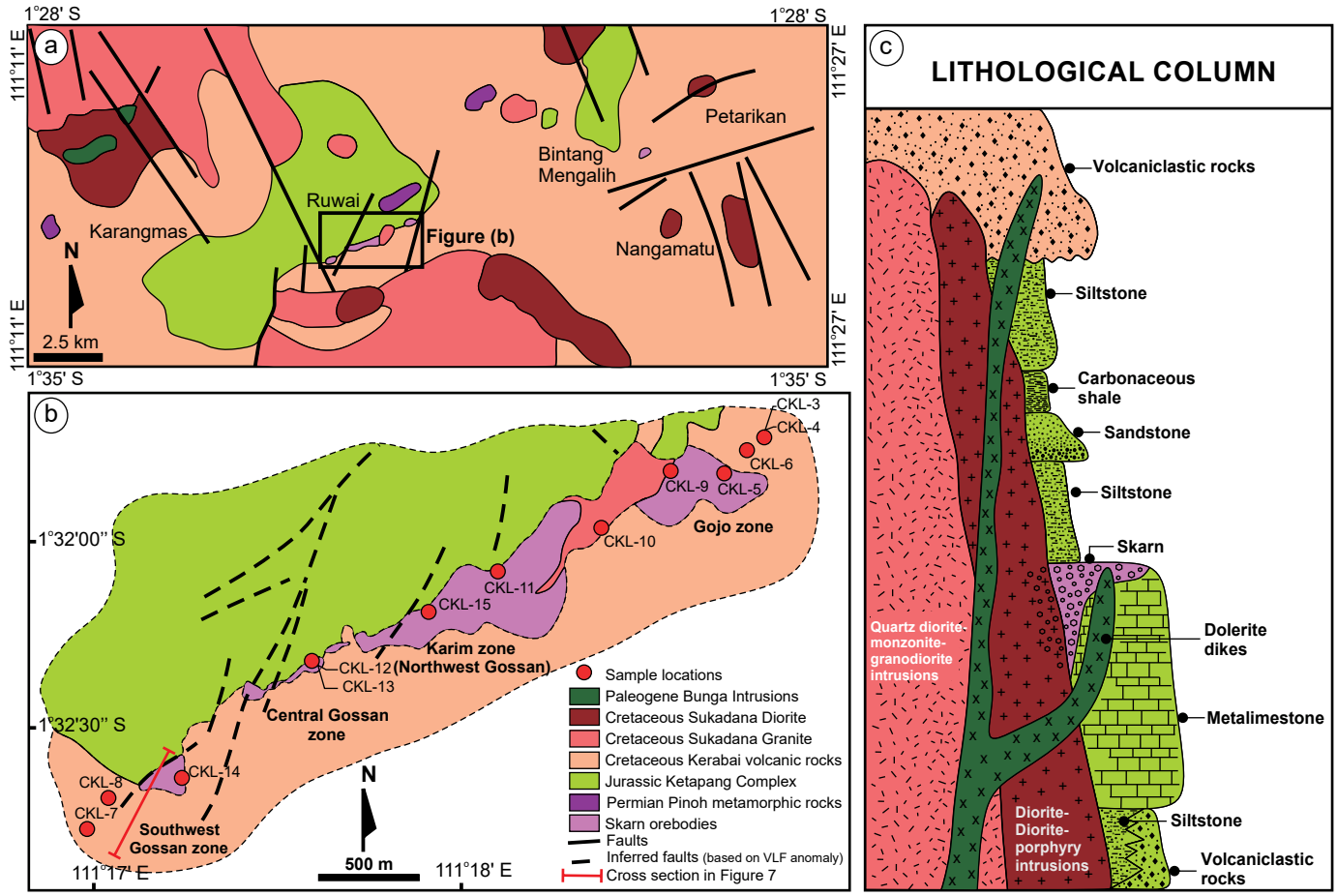

Fig. 2. Geologic maps (a, b) and schematic lithological column (c) of the Ruwai skarn deposit (modified after J.N.R. Ayson, unpub. report, 1997; D. Cooke and P. Kitto, unpub. report, 1997; Simbolon, et al., 2019). VLF = very low frequency.

have also been observed. Tsumoite was identified as rare infill between pyrite grains and associated with magnetite mineralization.

The skarn and orebodies are typically found along the contact of the intrusion with siltstone and marble and are controlled by a NW-trending anticline (Fig. 7). The endoskarn mostly occurs around Gojo and Karim in the form of massive garnet-epidote-magnetite with some relict igneous textures preserved (Simbolon et al., 2019). Toward the distal zone (Central and Southwest Gossan zones), the intrusions mostly occur as a smaller dike in which endoskarn is not well developed, although some partial replacement by garnet-epidote has occurred. Exoskarn is not continuous along the contact between marble and intrusions at Ruwai because of to the composition of the marble, which locally contains abundant siliciclastic impurities, presumably a marl/calcareous siliciclastic protolith (Idrus et al., 2011; Setijadji et al., 2011).

Structures in the ore field have been revealed by ground magnetic and very low frequency (VLF) geophysical surveys and include mainly NE-NNE–trending, NW- or SE-dipping faults and crosscutting NNW-trending dextral strike-slip faults (locally WSW-trending in the Ruwai ore zone). The NE-NNE–trending faults are related spatially and temporally to skarn mineralization (pre-/syn-ore), whereas the NNW- and WSW-trending ones may have formed post-ore and dissected and/or transposed the orebody into four ore zones (Idrus et al., 2011; Simbolon et al., 2019). A prominent NNE-trending, steeply SE-dipping, and sinistral fault (300- to 350-m displacement) located between the Ruwai and Southwest Gossan zones terminates the mineralization to the west (D. Cooke and P. Kitto, unpub. report, 1997; Simbolon et al., 2019).

Samples and Analytical Methods

Petrography (optical microscope and scanning electron microscopy-energy dispersive X-ray spectrometry; SEM-EDS)

A total of 60 samples consisting of skarn, massive ores, intrusions, and marble collected from drill core and outcrop were prepared as thin and polished sections for mineralogical characterization. Petrographic observations were performed on a Nikon Eclipse LV100N POL polarizing microscope. Several representative polished rock mounts were prepared for the advanced mineral identification and characterization system (AMICS) at the Central Science Laboratory, University of Tasmania. The analysis used a tungsten source FEI MLA650 scanning electron microscope equipped with a Bruker Quantax Esprit EDS system and two XFlash 5030 SDD detectors with 133-eV energy resolution. Analytical conditions include 20-kV accelerating voltage and 7-nA beam current, which

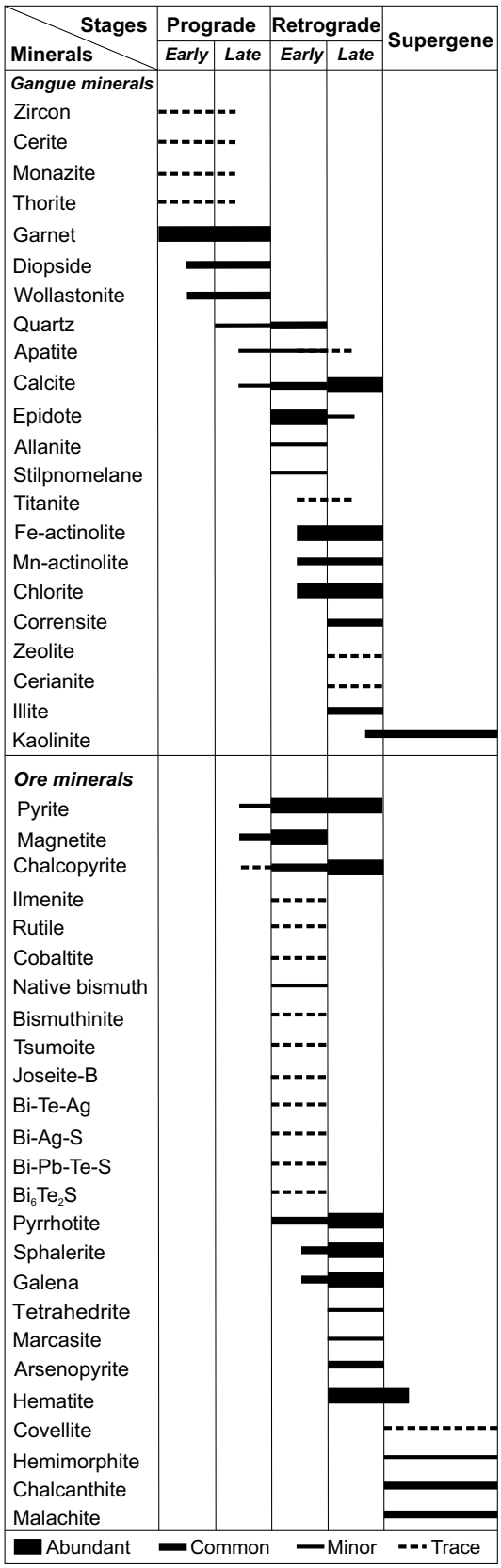

Fig. 3. Mineral paragenesis of the Ruwai skarn deposit, composed of three main mineralization stages including prograde, retrograde, and supergene phases. The main mineralization occurred during the retrograde phase.

yielded ~600,000 cps total EDS X-ray intensity and 30% dead time on quartz. Automated mineral identification was done with the Bruker AMICS software package (version 3.0.0.249) and the following setting: block sample mode, particle measurement mode, 1,024- × 1,024-pixel single-frame resolution, 1.536-mm single-frame field of view (equiv 1.5- × 1.5-µm pixel size), 16-µs backscattered electron (BSE) imaging pixel dwell time, 2% frame intersect, 5-ms EDS acquisition time, 3-µm EDS minimum segment size, 95 segmentation gray-level factor, 70 segmentation area factor, 50% classification reliability factor. A representative area of 3 × 3 frames (total nine frames) on each sample was mapped.

Electron probe microanalysis (EPMA)

Electron probe microanalysis was carried out on garnet and titanite selected for geochronological and trace element analysis, as well as on pyroxene, chlorite, and epidote. Garnet, epidote, and titanite analysis was performed using a JEOL JXA-8230 SuperProbe at Akita University, whereas pyroxene and chlorite analysis was performed using a JEOL JXA-8900R electron probe microanalyzer at RWTH Aachen University. The analytical conditions were set as follows: voltage 15 kV, beam current 20 nA, beam size 5 µm, and peak-background measurement time 20 and 10 s; the X-ray used was Kα for all elements. Several natural minerals were used as standards, including quartz (Si), periclase (Mg), hematite (Fe), wollastonite (Ca), orthoclase (K), corundum (Al), albite (Na), rhodonite (Mn), pyrophanite (Ti), and eskolaite (Cr). The lower detection limits are below 0.02 wt %. The raw results were processed using ZAF correction. Iron speciation (Fe^{2+} and Fe^{3+}) was computed following the procedure of Droop (1987).

Laser ablation-inductively coupled plasma-mass spectrometry (LA-ICP-MS)

Zircon analysis: Fifteen intrusions and volcanic rocks were prepared for whole-rock geochemical and zircon U-Pb-Hf isotope analyses. Zircons were separated by conventional density and magnetic separation techniques. After imaging with optical microscopy and cathodoluminescence (CL), the zircons were U-Pb dated at the Guangzhou Institute of Geochemistry, Chinese Academy of Sciences (GIGCAS). The analyses were performed on a RESOlution S-155 laser ablation system coupled with an Agilent 7900 ICP-mass spectrometer, using a 29-µm spot size. The analytical conditions include repetition rate of 5 Hz and laser fluence of 4 J cm^{-2}. Each analysis consisted of a 20- to 30-s background signal acquisition (laser off), followed by a 50-s sample data acquisition (laser on). Helium was used as the carrier gas (0.8 L min^{-1}), with NIST 610 glass used for element quantification and Si (69.7 ± 0.5 wt %) as the analyte of known concentration (internal standard). The primary 91500 zircon (Wiedenbeck et al., 1995) and secondary Plesovice zircon (Sláma et al., 2008) reference materials were analyzed between every five unknowns, and our Plesovice zircon analyses yielded a weighted mean $^{206}Pb/^{238}U$ age of 342.1 ± 1.1 Ma (mean square of weighted deviates [MSWD] = 0.66, n = 181) consistent (<3% error) with the recommended value (isotope dilution-thermal ionization mass spectrometry [ID-TIMS]: 337.13 ± 0.37 Ma; Sláma et al., 2008). Offline selection, background and analyte signal integration, quantitative calibration, and time-drift correction were performed with

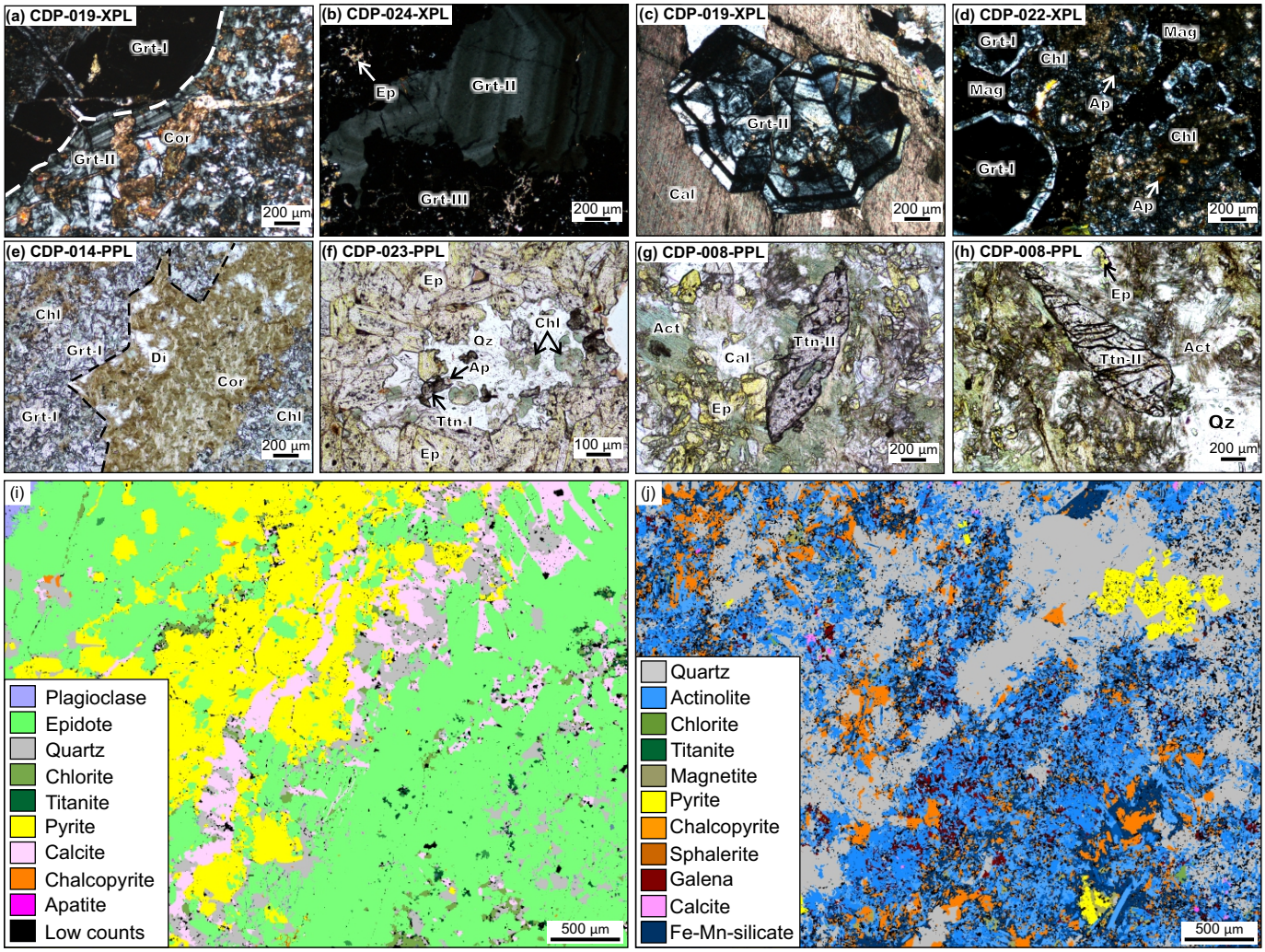

Fig. 4. Photomicrographs of skarn minerals assemblages. (a-d) Mode of occurrence of garnet in prograde stage. (e) Replacement of garnet and pyroxene by chlorite-corrensite. (f-h) Mode of occurrence of titanite in retrograde stage. (i, j) Advanced mineral identification and characterization system (AMICS) mapping images of retrograde skarn assemblages with coexistence of sulfide minerals. Abbreviations: Act = actinolite, Ap = apatite, Cal = calcite, Chl = chlorite, Cor = corrensite, Di = diopside, Ep = epidote, Grt = garnet, Mag = magnetite, Qz = quartz, Ttn = titanite.

the ICPMSDataCal v.10.1 software (Lin et al., 2016). Only zircon spots with (nearly) concordant ages (<15% discordance) were used for the age calculation, and the data were plotted on Wetherill concordia plots using IsoplotR v.4.2 (Vermeesch, 2018). The weighted mean $^{206}Pb/^{238}U$ age is reported to represent the crystallization age.

Zircon Hf-isotope analyses (details of results are provided in App. Table A1) were performed at GIGCAS on a RESOlution M-50 193-nm laser ablation system coupled with a Thermo Scientific Neptune Plus multicollector (MC)-ICP-mass spectrometer. The spot analysis was done on or near the U-Pb spot in the same age domain (with no inherited core or growth rim shown in CL images), with 4-J cm^{-2} energy density, 6-Hz repetition rate, 45-µm spot size, and helium carrier gas (0.8 L min^{-1}). Each spot analysis consisted of 400 cycles (integration time = 0.131 s/cycle), comprising 28 s of gas blank background measurement (laser off) and 30 s of sample signal collection (laser on). The zircon standard Penglai (Li et al., 2010) was analyzed twice every hour to check the reliability of the method, and its results were within ±1.5 ε_{Hf} unit error of the recommended values (Li et al., 2010). Plesovice zircon was analyzed as unknown for quality control. The ^{180}Hf gas blank was below 0.2 mv, with ^{173}Yb and ^{175}Lu used to correct the isobaric interference of ^{176}Yb and ^{176}Lu on ^{176}Hf. Natural $^{176}Yb/^{173}Yb$ (0.79381) and $^{176}Lu/^{175}Lu$ (0.02656) ratios were used in the correction (Segal et al., 2003). The mass bias factor of Yb was calculated from the measured $^{173}Yb/^{171}Yb$ and the natural ratio (1.13268), while those of Lu and Yb are assumed to be the same. The $^{176}Hf/^{177}Hf$ mass bias was normalized to $^{179}Hf/^{177}Hf$ (0.7325) with an exponential law. All the uncertainties reported in absolute values for both U-Pb and Hf data and detailed instrumentation, and for the final age calculation (weighted mean $^{206}Pb/^{238}U$ age) the uncertainty was reported as 2σ without | with σ_{sys}. Analytical procedures and data processing protocols followed those described by Xu et al. (2019, and references therein).

Garnet and titanite analysis: Three types of garnet and two types of titanite from five representative samples of garnet-

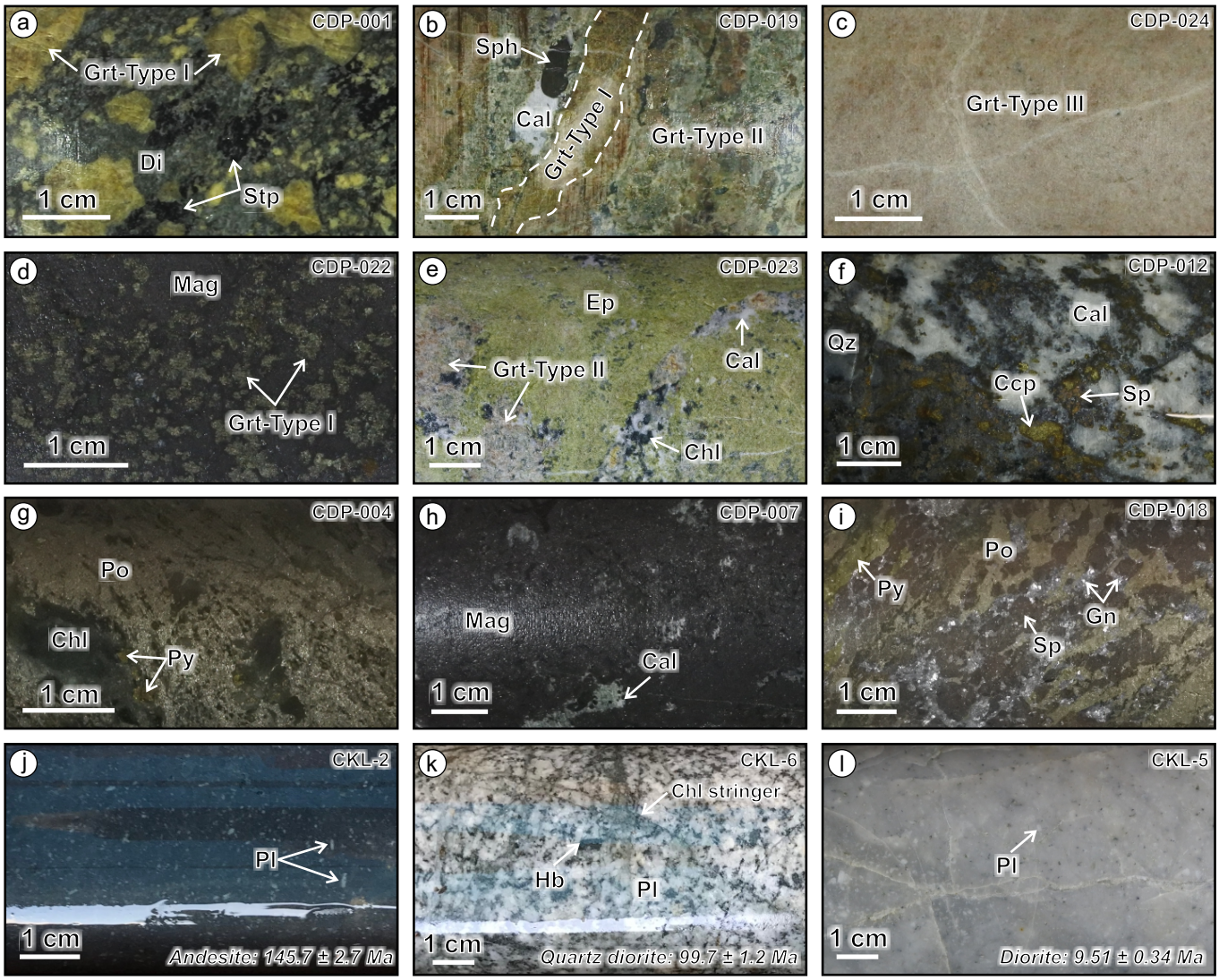

Fig. 5. Representative core samples from the Ruwai skarn deposit. (a) The occurrence of stilpnomelane associated with type I garnet and diopside. (b) Coexistence of type I and type II garnet. (c) Massive fine-grained type III garnet. (d) Magnetite mineralization associated with type I garnet. (e) Type II garnet represents the prograde stage and is overprinted by epidote-chlorite-calcite from the retrograde stage. (f) Disseminated chalcopyrite-sphalerite within marble. (g) Massive pyrrhotite ore with minor occurrence of chlorite-pyrite. (h) Massive magnetite ore with minor occurrence of calcite. (i) Massive sulfide ore consists of pyrite-pyrrhotite-sphalerite-galena. (j) Early Cretaceous andesite with fine-grained plagioclase. (k) Late Cretaceous quartz diorite with coarse-grained plagioclase-hornblende and chlorite stringers. (l) Late Miocene silicified diorite with fine-grained plagioclase relicts. Mineral abbreviations: Cal = calcite, Ccp = chalcopyrite, Chl = chlorite, Di = diopside, Ep = epidote, Gn = galena, Grt = garnet, Hb = hornblende, Mag = magnetite, Pl = plagioclase, Po = pyrrhotite, Py = pyrite, Qz = quartz, Sp = sphalerite, Stp = stilpnomelane.

epidote skarn were selected for in situ geochronological and geochemical analysis. They were analyzed by LA-ICP-MS at the Institute of Geochemistry and Petrology, ETH Zurich, Switzerland, using a RESOlution S-155 (ASI/Applied Spectra) 193-nm ArF excimer laser ablation system attached to an Element XR (Thermo) sector-field ICP-mass spectrometer. A total of 244 points for garnet and 130 points for titanite were selected for U-Pb dating and simultaneous trace element analysis. For garnet analysis, the same garnet type from different samples is combined for age calculation. The laser beam diameters were set at 51 µm for garnet and 29 µm for titanite. The laser fluence and repetition rate for garnet were set at 2 J/cm^2 and 5 Hz, whereas for titanite they were set at 2 J/cm^2 and 4 Hz. The trace element compositions of the garnet were calibrated against the GSD-1G standard reference, using Si as the internal standard, whereas Mali grandite (Seman et al., 2017) was used as primary reference material for U-Pb dating. Accuracy was assured by analyzing the following as unknowns: Jaco Lake (Seman et al., 2017; 35 ± 2 Ma, ^{206}Pb/^{238}U age) and QC04 (Deng et al., 2017; 130 ± 1 Ma, ^{206}Pb/^{238}U age), with the results from this study for QC04 being weighted average of ^{206}Pb/^{238}U age = 129.5 ± 3 Ma (2s, MSWD = 0.68, n = 40). The trace elements of titanite were calibrated against the NIST-610 standard, using Ca as the internal standard, whereas MKED1 titanite (Spandler et al., 2016) was used as primary reference material for U-Pb dating. Accuracy of titanite ages

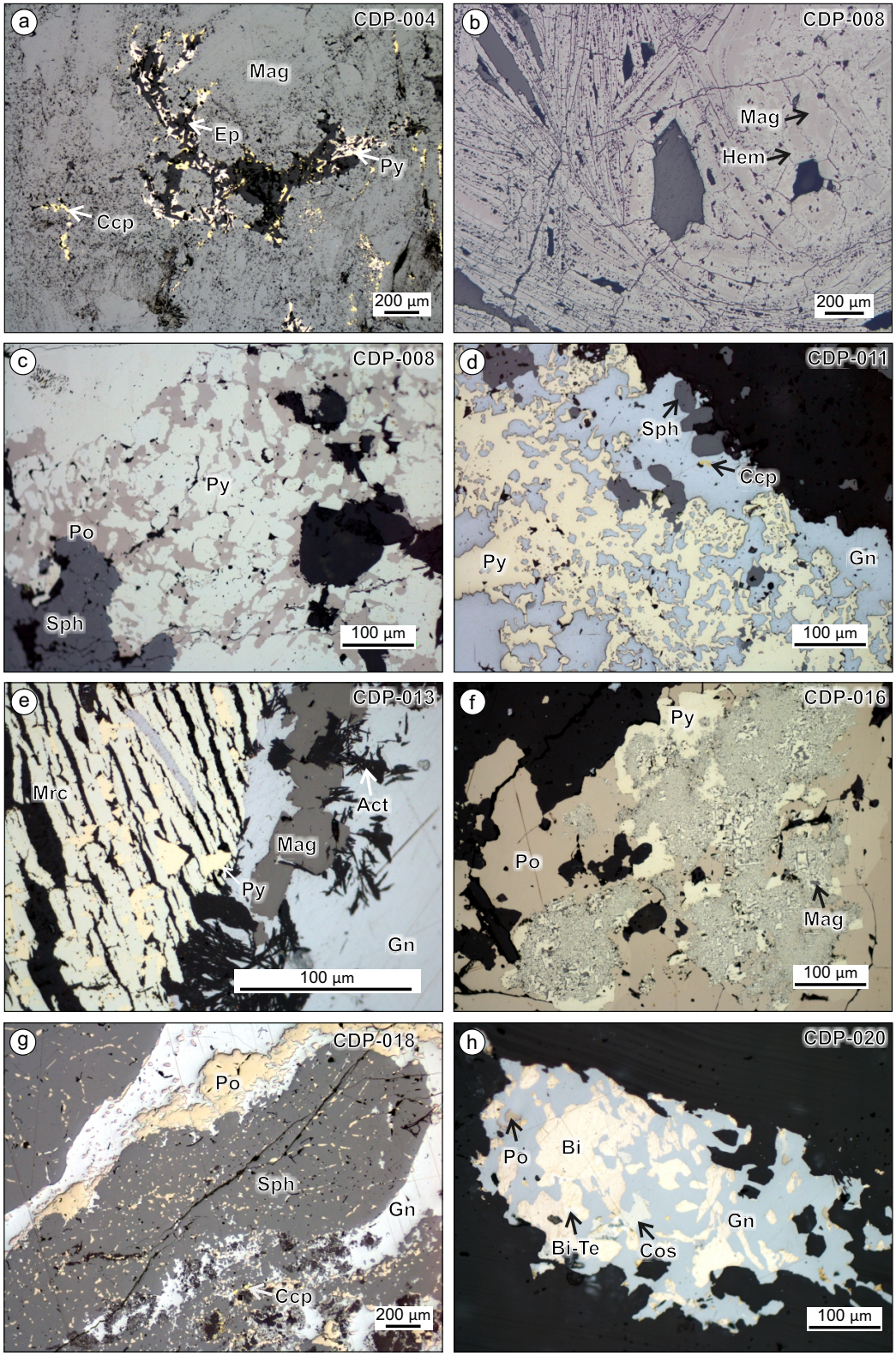

Fig. 6. Photomicrographs of ore mineral assemblages. (a) Massive magnetite mineralization with minor occurrences of chalcopyrite and pyrite. (b) Replacement of magnetite by hematite. (c) Replacement of pyrite by pyrrhotite. (d) Pyrite replacement by galena. (e) Lamellar marcasite with euhedral pyrite associated with galena-magnetite and actinolite. (f) Oxidation of pyrite by magnetite which then enveloped by pyrrhotite. (g) Coexistence of pyrrhotite-galena-sphalerite-chalcopyrite in massive sulfide. (h) Coexistence of bismuth-bearing minerals-galena-pyrrhotite with exsolution texture. Mineral abbreviations: Act = actinolite, Bi = native bismuth, Ccp = chalcopyrite, Cos = cosalite, Ep = epidote, Gn = galena, Hem = hematite, Mag = magnetite, Mrc = marcasite, Po = pyrrhotite, Py = pyrite, Sph = sphalerite.

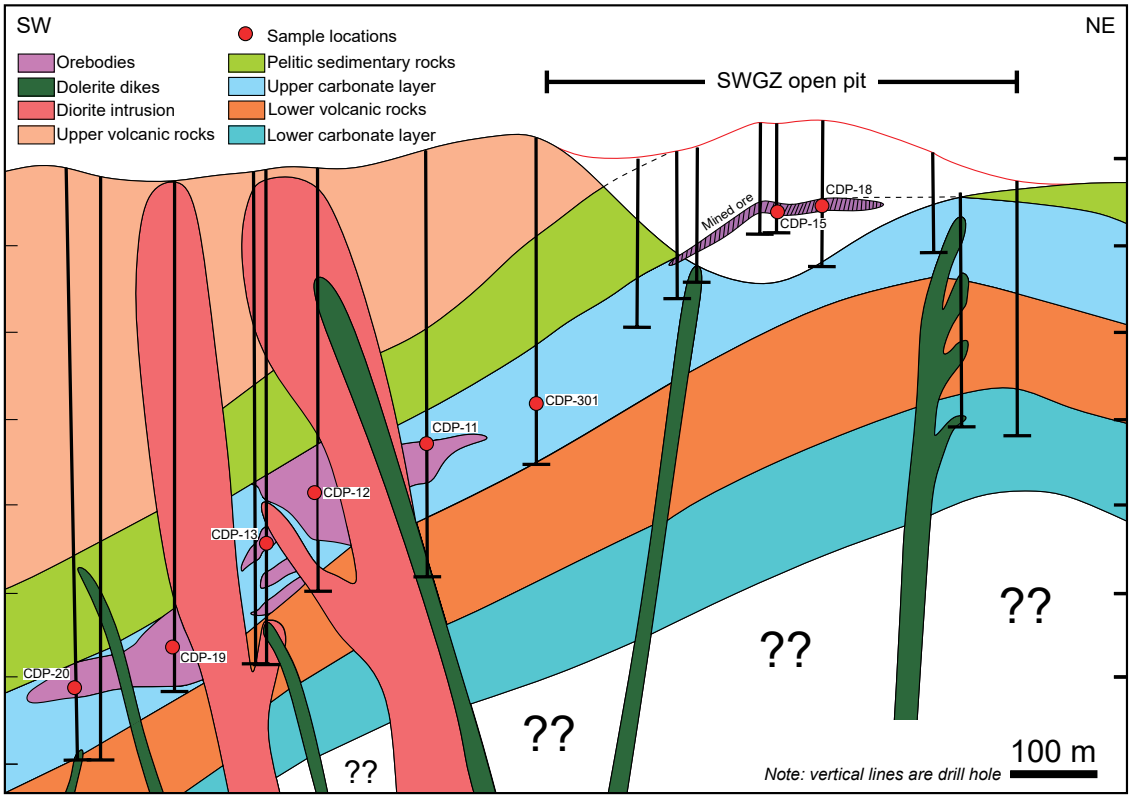

Fig. 7. Schematic cross section along the Southwest Gossan zone (SWGZ) shows the stratigraphically and structurally controlled occurrences of orebodies (data from PT Kapuas Prima Coal, Tbk., 2020).

was assured by analyzing the following as unknowns: 94-35 (51.5 ± 0.7 Ma) and BLS (same locality as BLR-1; 1049.9 ± 1.3 Ma; Aleinikoff et al., 2007), Otter West (147.9 ± 1.2 Ma; Butler et al., 2002), and Ecstall West (91.5 ± 1.0 Ma; Butler et al., 2002) with the result of this study for Otter West being a Tera-Wasserburg intercept age of 150.5 ± 5.5 Ma (MSWD = 2, n = 7). All data are available in Appendix Tables A2 and A3, including metadata tables with all relevant parameters after Horstwood et al. (2016). All the uncertainties are reported as absolute values both for garnet and titanite.

Data reduction was completed using Iolite 4.0 software (Paton et al., 2011; Petrus and Kamber, 2012). Common Pb corrections were not applied due to the heterogeneous distribution and high variability of common Pb. Garnet and titanite U-Pb ages were determined using linear regressions on Tera-Wasserburg concordia plots constructed using IsoplotR v.4.2 (Vermeesch, 2018), and the lower intercept is reported to represent the crystallization age. For trace element quantification, Iolite 4.0 was used with Si (18.7% for garnet) and Ca (19.25 wt % for titanite) as the known element (internal standard) for the same integration intervals used for dating. All geochemical data visualization including those obtained from EPMA analysis were constructed using ioGAS software.

Re-Os analysis

In this study, both sulfides (i.e., pyrite, pyrrhotite, chalcopyrite, and sphalerite) and magnetite were used. About 4 g of each mineral were manually separated and crushed using an agate mortar and pestle. Sulfides and magnetite were collected from both massive and disseminated ore samples. For Re-Os isotope measurements, this study employed MC-ICP-MS combined with the sparging introduction method that introduced vaporized OsO_4 into the instrument by bubbling Ar sample gas in the sample solution (Hassler et al., 2000; Schoenberg et al., 2000; Norman et al., 2002; Nozaki et al., 2012; Kimura et al., 2014). This method achieved high sample throughput and low blanks. However, it was important to ensure that the sample matrix and Os and Re in the sample were perfectly oxidized for accurate analysis by MC-ICP-MS with the sparging method. Re-Os analysis of sulfides requires more oxidants than other oxide-dominated geologic materials (e.g., pelagic sediment) because a large amount of oxidant is consumed in the oxidative decomposition of sulfides. Therefore, we added $HClO_4$ to inverse aqua regia (Gao et al., 2019; Ohta et al., 2022). Our analytical method followed those previously reported (Kimura et al., 2014; Ohta et al., 2022) with some modification for use of $HClO_4$. The powdered sample was dried at 40°C for at least 24 h before weighing. Approximately 0.4 g of powdered sample was weighed and spiked with ^{185}Re and ^{190}Os in a thick-walled Carius tube (Shirey and Walker, 1995). Then 1 mL HCl, 1 mL $HClO_4$, and 3 mL HNO_3 (Ohta et al., 2022) were added, in this order. The Carius tube was sealed and then heated in an oven at 220°C for 24 h. After cooling, the solution was transferred to a 15-mL centrifuge tube and centrifuged at 3,000 rpm for 5 min. The supernatant was filtered and diluted with Milli-Q water to bring the total volume to 15 mL. The Os isotope ratios were measured with MC-ICP-MS (Neptune Plus; Thermo Fisher Scientific)

at Ocean Resources Research Center for Next Generation (ORCeNG) of Chiba Institute of Technology (CIT) combined with sparging sample introduction. The instrumental mass bias was corrected by normalizing with $^{192}Os/^{188}Os = 3.08271$ (Luck and Allègre, 1983) based on the exponential law. Measurements of sphalerite and magnetite samples, which contained relatively high concentration of Os, were performed by multiple Faraday cup detectors, and those of chalcopyrite, pyrite, pyrrhotite, which contained low concentration of Os, and procedural blank sample were performed by multiple ion-counting detectors (Ohta et al., 2022). Os concentrations were determined by the isotope dilution method and corrected for Os in the blank sample, which was 0.033 ± 0.003 pg with a $^{187}Os/^{188}Os$ ratio of 0.345 ± 0.005 (1 standard error [S.E.]).

After the Os measurements were completed, the solutions were heated to remove remaining Os. Rhenium in the sample solutions was purified by two-step chromatography with Muromac AG1-X8 anion exchange resin (Morgan et al., 1991; Kato et al., 2005) and then dissolved in 1 mL 3% HNO_3 solution. Finally, 15 µL 10 ng/g Ir standard solution was added for the correction of mass bias effect (Ohta et al., 2022). For Re isotope analysis, the Re-bearing solution was introduced into the glass ICP torch through a self-aspirating PFA nebulizer and a glass spray chamber. The instrumental mass bias effect was corrected by external correction method using $^{193}Ir/^{191}Ir$ ratio with empirical calibration of mass bias coefficient of $^{187}Re/^{185}Re$ (Ohta et al., 2022). Concentrations of Re were determined by isotope dilution and corrected for Re in the blank samples, the average of which was 1.66 ± 0.02 pg (1 S.E.). The Re-Os ages were determined using linear regressions (model 3: maximum likelihood with overdispersion) constructed using IsoplotR v.4.2 (Vermeesch, 2018).

Whole-rock geochemical analysis

In this study, both Cretaceous (n = 7) and Miocene (n = 4) samples of intrusions were selected for geochemical analysis at the Bureau Veritas Laboratory in Vancouver, Canada. The rock samples were crushed and pulverized to 200 mesh, and powdered samples were digested by Li borate fusion (details of results and detection limits are provided in App. Table A4). Concentrations of 10 major element oxides and 56 trace elements (including REEs) were measured with ICP-atomic emission spectroscopy (AES) and ICP-MS, respectively. The ioGAS-REFLEX program (version 7.4.2) was used for data analysis and visualization.

Stable isotopic analysis

Sulfur isotope data were obtained from sulfides (pyrite, galena, sphalerite, chalcopyrite, and pyrrhotite) and one sulfate (chalcanthite) sample. A total of 13 sulfide samples were sent to the Laboratory of Geochemistry and Mineral Resources, Karlsruhe Institute of Technology (KIT), Germany, for in situ S isotope analyses. The analyses were done using an IRMS Isoprime with EA Eurovector instrument. Three calibration standards were used including silver sulfide of IAEA-S-1 and IAEA-S-3 as well as barium sulfate of NBS-127. Additional sulfur isotope analyses from 18 samples were conducted by conventional procedures at Akita University, Japan. About 20 mg of sulfides (n = 17) and 300 mg of sulfate (n = 1) were separated by handpicking. Sulfide minerals were prepared with the procedure of Yanagisawa and Sakai (1983). In the case of chalcanthite, the preparation was similar to the procedure for anhydrite/gypsum including dilution with HCl and then addition of $BaCl_2$. The sulfur isotope compositions were measured using a Thermo Fisher Scientific Delta V Advantage isotope ratio monitoring mass spectrometer. Three standards were used including barium sulfate of IAEA-SO-5, IAEA-SO-6, and NBS-127 for calibration. All results were reported with respect to Vienna-Canyon Diablo Troilite (V-CDT) with the accuracy for sulfide of ±0.2‰ and for sulfate of ±0.4‰.

A total of 15 calcite samples including those from marble host rock and prograde and retrograde skarn were prepared for C-O isotope analysis. Carbon and oxygen isotopes were measured in manually separated samples of calcite (about 20 mg). The isotopes were analyzed at GNS Isotope Laboratory, New Zealand, with the GVI IsoPrime carbonate preparation system at a reaction temperature of 25°C for 24 h and run via dual inlet on the IsoPrime mass spectrometer. All results are reported with respect to Vienna-Pee Dee Belemnite (V-PDB), normalized to internal standards GNS Marble with reported values of 2.04‰ for $\delta^{13}C$ and –6.40‰ for $\delta^{18}O$. The external precision for these measurements is better than 0.1‰ for $\delta^{13}C$ and 0.2‰ for $\delta^{18}O$.

Chemical Composition of Skarn Minerals

Garnet

At least three texturally and chemically different garnets were observed (Fig. 8): (1) type I—isotropic andradite ($Ad_{41–98}Gr_{0–48}$, where Ad = andradite and Gr = grossular), (2) type II—anisotropic andradite-grossular ($Ad_{60–96}Gr_{0–33}$), and (3) type III—isotropic grossular ($Ad_{8–30}Gr_{62–86}$). Details of chemical compositions are provided in Appendix Tables A2 and A5. Type I garnets are characterized by andradite-rich cores ($Ad_{71–98}Gr_{0–21}$) and more grossular-rich rims ($Ad_{41–70}Gr_{18–48}$). Type II garnets are birefringent and characterized by oscillatory compositional zoning toward the rim. Generally, the cores of type II garnets have similar compositions to the rims of type I garnets ($Ad_{51–76}Gr_{20–42}$). The transition to the rim is marked by the occurrence of a distinct, narrow andradite-rich band that is compositionally similar to the core of type I garnets ($Ad_{90–92}Gr_{1–3}$). Type III garnets are characterized by relatively homogeneous grossular-rich compositions (core: $Ad_{10–24}Gr_{68–82}$; rim: $Ad_{8–30}Gr_{62–86}$) from cores to rims, although BSE images indicate the occurrence of a fine zoning pattern that was not resolved by our chemical traverses.

In terms of trace element contents, the total REE and HFSE contents vary between types of garnet, with type III garnets having the highest and type I having the lowest total REEs and HFSEs (Fig. 9). In C1 chondrite-normalized plots (Fig. 10), the cores of type I garnets are enriched in light (L)REEs over heavy (H)REEs and have strong positive Eu anomalies, whereas the rims are typically depleted in LREEs compared to HREEs and have negative Eu anomalies. Similar to the rims of type I, the cores of type II are also depleted in LREEs with negative Eu anomalies, and the HREE patterns are relatively flat. In andradite bands of type II garnets, the REE patterns are similar to those of the cores of type I. The rims of type I show strongly depleted LREEs and more enriched HREE patterns without any significant Eu anoma-

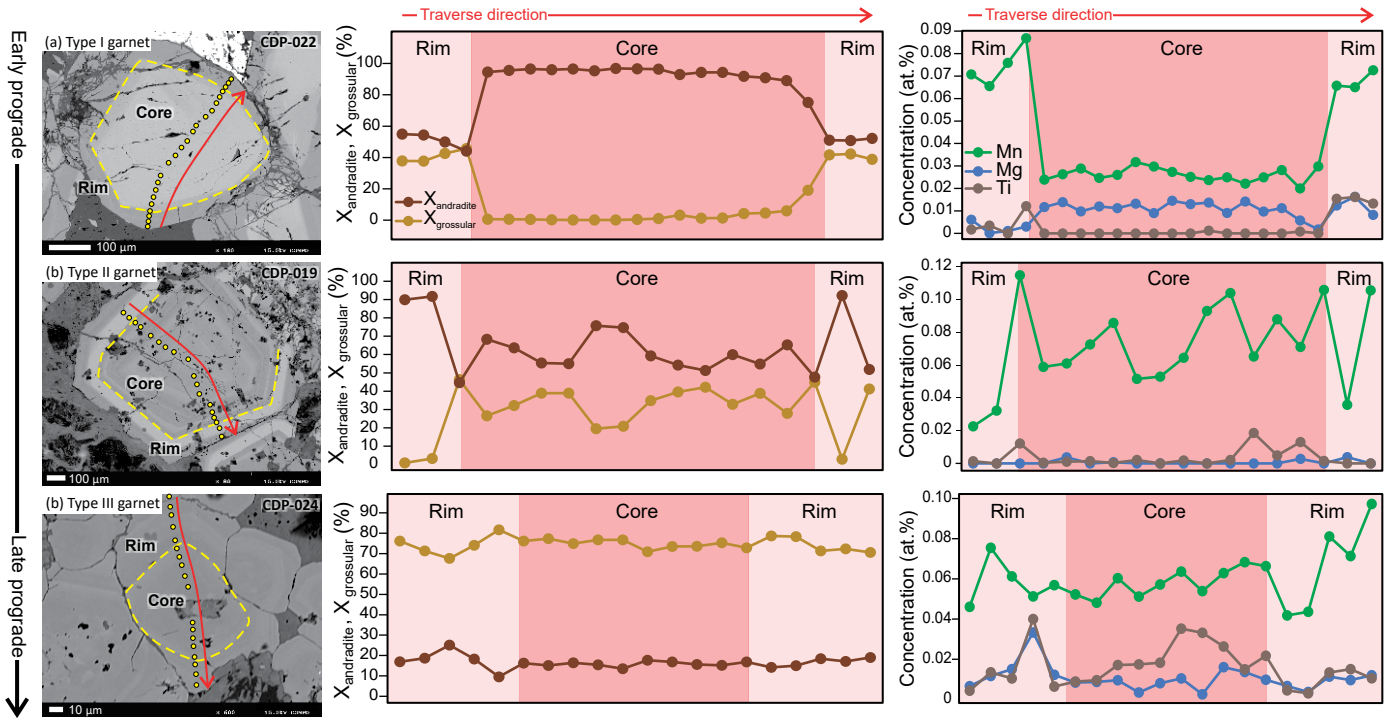

Fig. 8. Traverse spot analysis of three garnet types found in the Ruwai skarn deposit, showing gradual changes of garnet major and trace elements composition from andradite rich to grossular rich.

lies. Strong LREE depletions were also observed in type III garnets. Type III garnets also have relatively flat HREE patterns and lack Eu anomalies. Overall, the Eu anomalies are negatively correlated with total HREEs but are positively correlated with Fe/Al ratios.

Pyroxene

Diopside was the only pyroxene observed in this study. Detailed chemical compositions are provided in Appendix Table A6. Although most pyroxene at Ruwai has been replaced by actinolite and/or chlorite because of retrograde alteration, some perfectly zoned pyroxene was observed locally (Fig. 11a-d). Generally, the pyroxene cores are characterized by higher Mg/Fe and lower Mn, Ti, Al, and Na than the rims (Fig. 11a-d).

Titanite

In this study we observed two types of titanite (Fig. 4f-h): (1) type I titanite is associated with Pb-Zn mineralization and (2) type II titanite is associated with Fe mineralization. Type II has lower MgO and higher Fe_2O_3 contents than type I (App. Table A3). The two titanite types have similar total HFSE and REE contents, although in C1 chondrite-normalized plots (Fig. 10d-e), they have different REE patterns. Type I titanite is characterized by LREE depletion, relatively flat HREE patterns with slight depletion from Er to Lu, and strong Eu anomalies. In comparison, type II titanite is characterized by depleted LREEs with flat HREE patterns and minor or no Eu anomalies.

Epidote

Two types of epidote group mineral have been identified at Ruwai, including allanite and epidote sensu stricto. Only epidote sensu stricto was chemically analyzed by EPMA (App. Table A7), and it can be divided compositionally into two types: (1) Al epidote, which has been irregularly overgrown by (2) Fe epidote (Figs. 11f, 12d). The Al epidote is mostly associated with Pb-Zn (galena-sphalerite) mineralization, whereas Fe epidote is associated with Fe (magnetite) mineralization.

Chlorite

Based on the classification of Zane and Weiss (1998), chlorite in this study can be divided into Fe chlorite (chamosite: avg FeO = 36.4 wt %, avg MgO = 3.0 wt %) and Mg chlorite (clinochlore: avg FeO = 21.0 wt %, avg MgO = 16 wt %; Fig. 12c). Chamosite is typically associated with massive sulfide mineralization, whereas clinochlore is associated with magnetite mineralization. Details of chemical compositions are provided in Appendix Table A8.

U-Pb Geochronology

U-Pb zircon ages and Hf isotopes

In this study, the 15 dated samples fall into several age groups, i.e., pre-Cretaceous, Early Cretaceous, Late Cretaceous, and late Miocene. The results are plotted in Figure 13 with all uncertainties reported at the 2σ level. Details of the isotopic ratios are provided in Appendix Table A9. In this study, the zircon Th/U ratio of all samples ranges from 0.13 to 3.61 with one zircon having anomalously high Th/U up to 8.44 (avg 1.20, n = 301).

Pre-Cretaceous basement: The oldest sample from Ruwai is the hornfels metavolcanic rock of the Matan Complex (CKL-12). The 10 zircons analyzed are medium to fine grained (20–

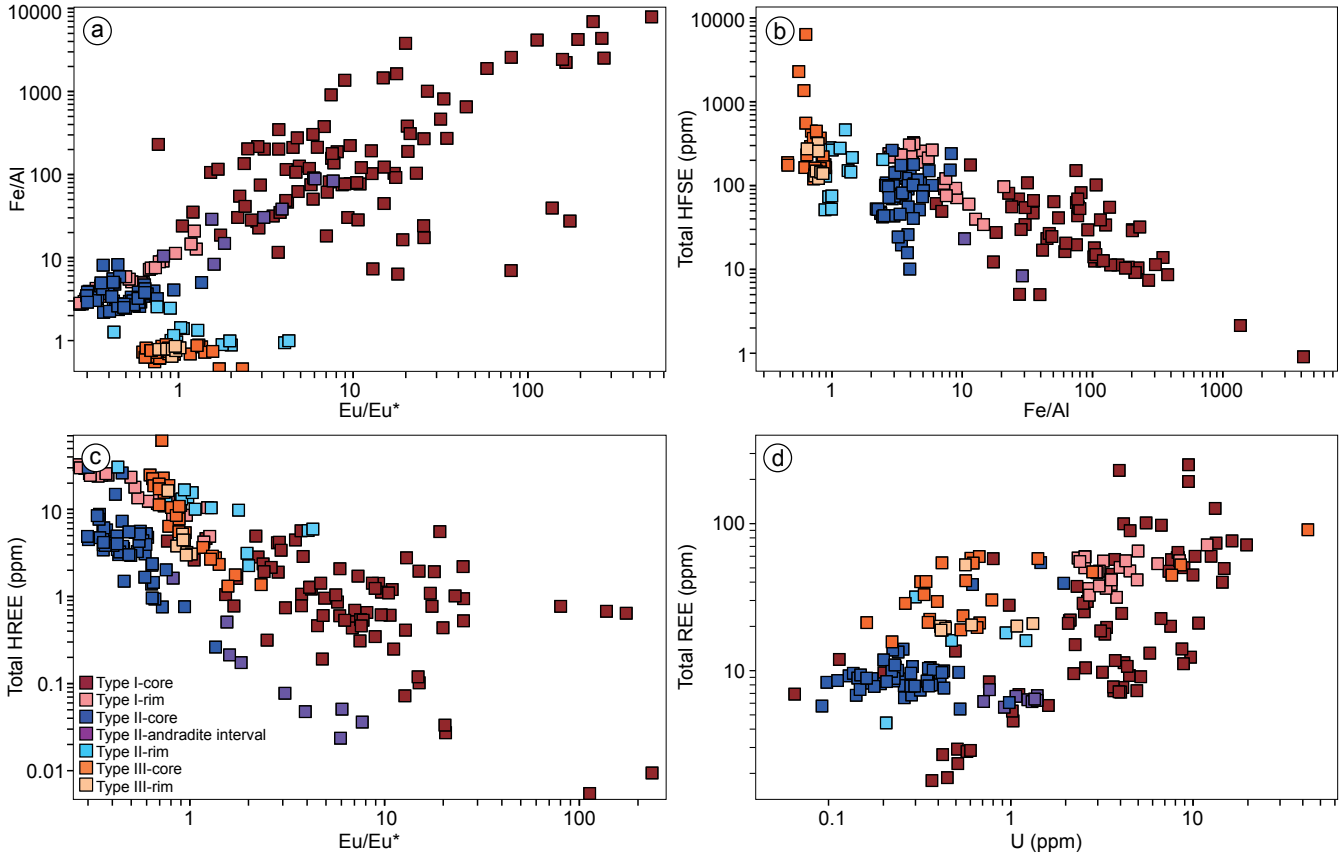

Fig. 9. Variation diagrams of trace elements in garnet. (a) Positive correlation of Eu anomaly with Fe/Al ratio. (b) Negative correlation of Fe/Al ratio with total high field strength elements (HFSEs: Sc, Y, Th, U, Pb, Zr, Hf, Ti, Nb, Ta). (c) Negative correlation of Eu anomaly with total heavy rare earth elements (HREEs). (d) Positive correlation of U with total REE contents.

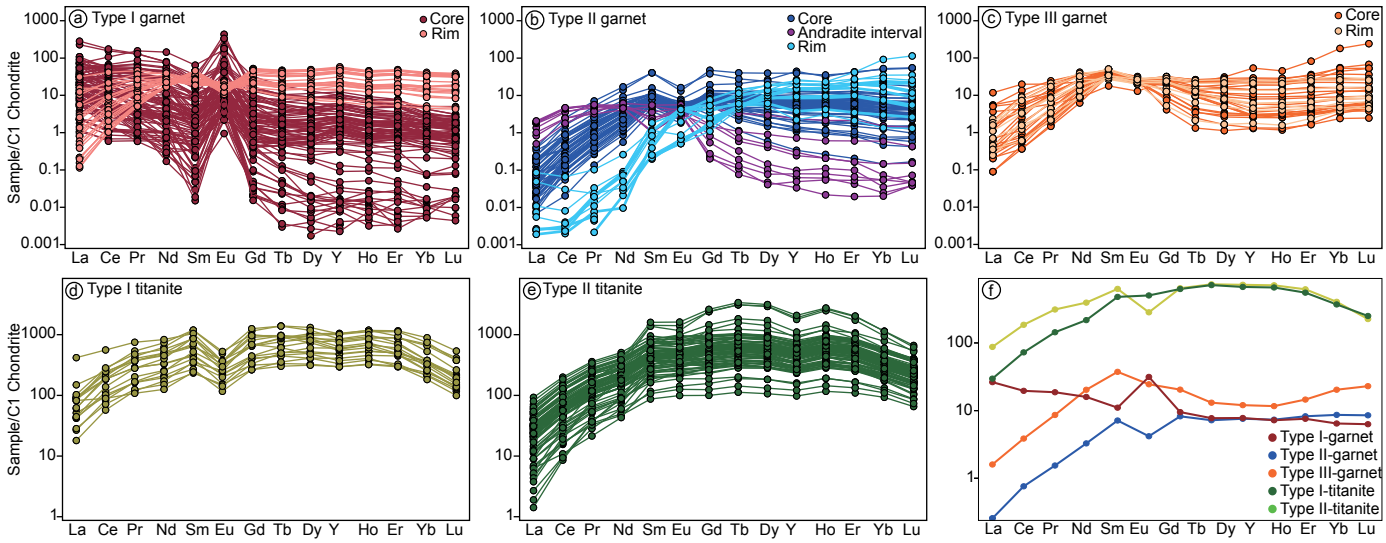

Fig. 10. C1 chondrite-normalized spider diagram of rare earth element contents in each types of garnet (a-c) and titanite (d, e) and their average values (f). (Normalization values from McDonough and Sun, 1995.)

80 μm long), are mostly subhedral-anhedral with rounded corroded margins, and display oscillatory or sector zoning in CL images (Fig. 14). The zircons are predominantly Siluro-Devonian (422.0–378.7 Ma; $\varepsilon_{Hf_{(t)}}$ = –1.9 to 6.3) and yielded a weighted average $^{206}Pb/^{238}U$ age of 403.3 ± 6.7 | 13.8 Ma (n = 9, MSWD = 2.2). As shown below, Siluro-Devonian zircons are present in many of the Cretaceous and Miocene igneous samples from the ore field.

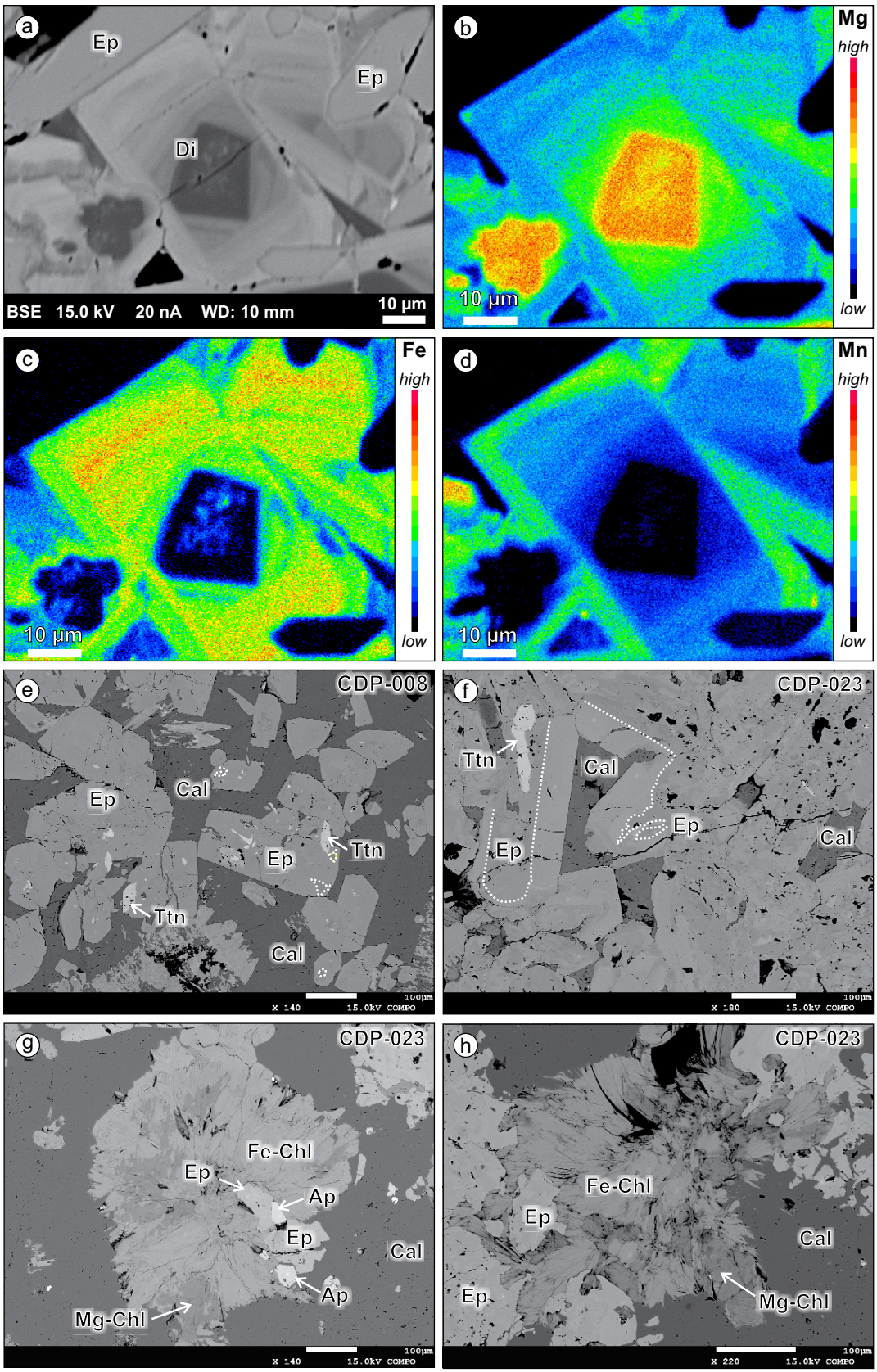

Fig. 11. Backscattered electron image and elemental maps of zoned clinopyroxene (a-d). Backscattered electron images of Fe and Al epidote (e, f) as well as Mg and Fe chlorite (g, h). Abbreviations: Ap = apatite, Cal = calcite, Di = diopside, Ep = epidote, Fe-Chl = Fe chlorite, Mg-Chl = Mg chlorite, Ttn = titanite.

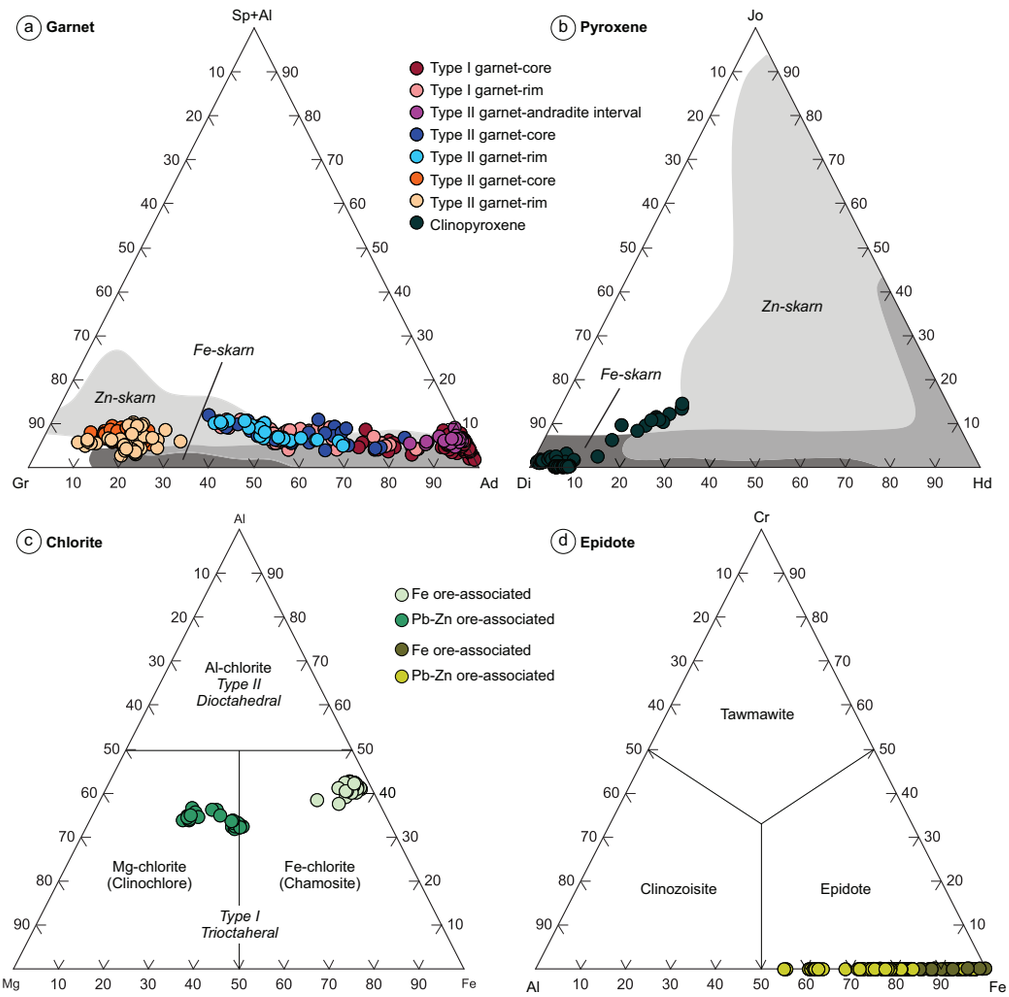

Fig. 12. Ternary classification diagrams of several minerals at Ruwai. (a, b) Garnet and clinopyroxene at Ruwai compared with typical garnet and clinopyroxene end members in skarn deposits (modified after Meinert et al., 2005). (c) Chlorite end-member classification (after Zane and Weiss, 1998). (d) Epidote end-member classification (after Franz and Liebscher, 2004). Abbreviations: Ad = andradite, Di = diopside, Gr = grossular, Hd = hedenbergite, Jo = johannsenite, Sp = sphalerite.

Early Cretaceous (ca. 144.6 and 107.6–106.2 Ma): The second oldest sample is an Early Cretaceous mineralized andesite (CKL-2). The zircons (n = 20) cluster around a Late Jurassic-Early Cretaceous age (150.6–141.3 Ma, $\varepsilon_{Hf_{(t)}}$ = 5–11.7, n = 8) and Siluro-Devonian age (424.0–392.1 Ma, $\varepsilon_{Hf_{(t)}}$ = –0.5 to 7.1, n = 9), with weighted average $^{206}Pb/^{238}U$ ages of 144.4 ± 2.7 | 5.1 Ma (MSWD = 0.7) and 411.8 ± 6.8 | 14.1 Ma (MSWD = 1.4), respectively. These ages likely reflect the andesite emplacement and crustal inheritance, respectively. Two Kerabai Volcanics samples, including a crystal-lithic andesitic tuff (CKL-7) and a dacite porphyry (CKL-8), yielded Early Cretaceous ages. Despite their different size (20–100 µm) and morphology (euhedral prismatic/tabular to subhedral; Fig. 14), all the zircons have similar Albian ages: CKL-7 has ages of 106.7 to 102.5 Ma (weighted avg $^{206}Pb/^{238}U$ age of 106.2 ± 0.6 | 3.3 Ma, n = 50, MSWD = 0.7), and $\varepsilon_{Hf_{(t)}}$ = –2.0 to 8.6, and CKL-8 has ages of 112.5 to 105.1 Ma (weighted avg age 107.8 ± 1.2 | 3.5 Ma, n = 20, MSWD = 0.4), with $\varepsilon_{Hf_{(t)}}$ = 2.4 to 6.3. These are interpreted as the andesite crystallization ages.

Late Cretaceous (ca. 99.8–97.0 Ma): A total of five samples belong to this group, including two granodiorites (CKL-4 and CKL-9), one monzonite (CKL-10), one quartz diorite (CKL-6), and one altered acid volcanic rock (CKL-13). Zircon grains from the granitoid samples (granodiorite, monzonite, and quartz diorite) are predominantly latest Early Cretaceous-Late Cretaceous (App. Table A9). Zircons of these ages are commonly coarse grained (many >100 µm) and display well-developed, occasionally multiphase oscillatory zoning (Fig. 14). The quartz diorite (CKL-6) has weighted average $^{206}Pb/^{238}U$ age of 100.0 ± 1.0 | 3.2 Ma (n = 20, MSWD = 1.1), and $\varepsilon_{Hf_{(t)}}$ = 4.9 to 10.3. The granodiorite samples have weighted average $^{206}Pb/^{238}U$ ages of 99.3 ± 1.1 | 3.2 Ma (n = 22, MSWD = 0.7, $\varepsilon_{Hf_{(t)}}$ = 4.1 to 10.9; CKL-9) and 96.9 ± 1.1 | 3.1 Ma (n = 21, MSWD = 0.6, $\varepsilon_{Hf_{(t)}}$ = 4.1 to 9.9; CKL-4), which are interpreted as magmatic ages; neither sample has inherited zircons. The monzonite sample has a weighted average $^{206}Pb/^{238}U$ age of 98.8 ± 1.2 | 3.2 Ma (n = 17, MSWD = 1.0, $\varepsilon_{Hf_{(t)}}$ = –2.8 to 11.0; CKL-10), interpreted as the magmatic age, and two xenocrystic zircons (155.3 and 1687.4 Ma). The

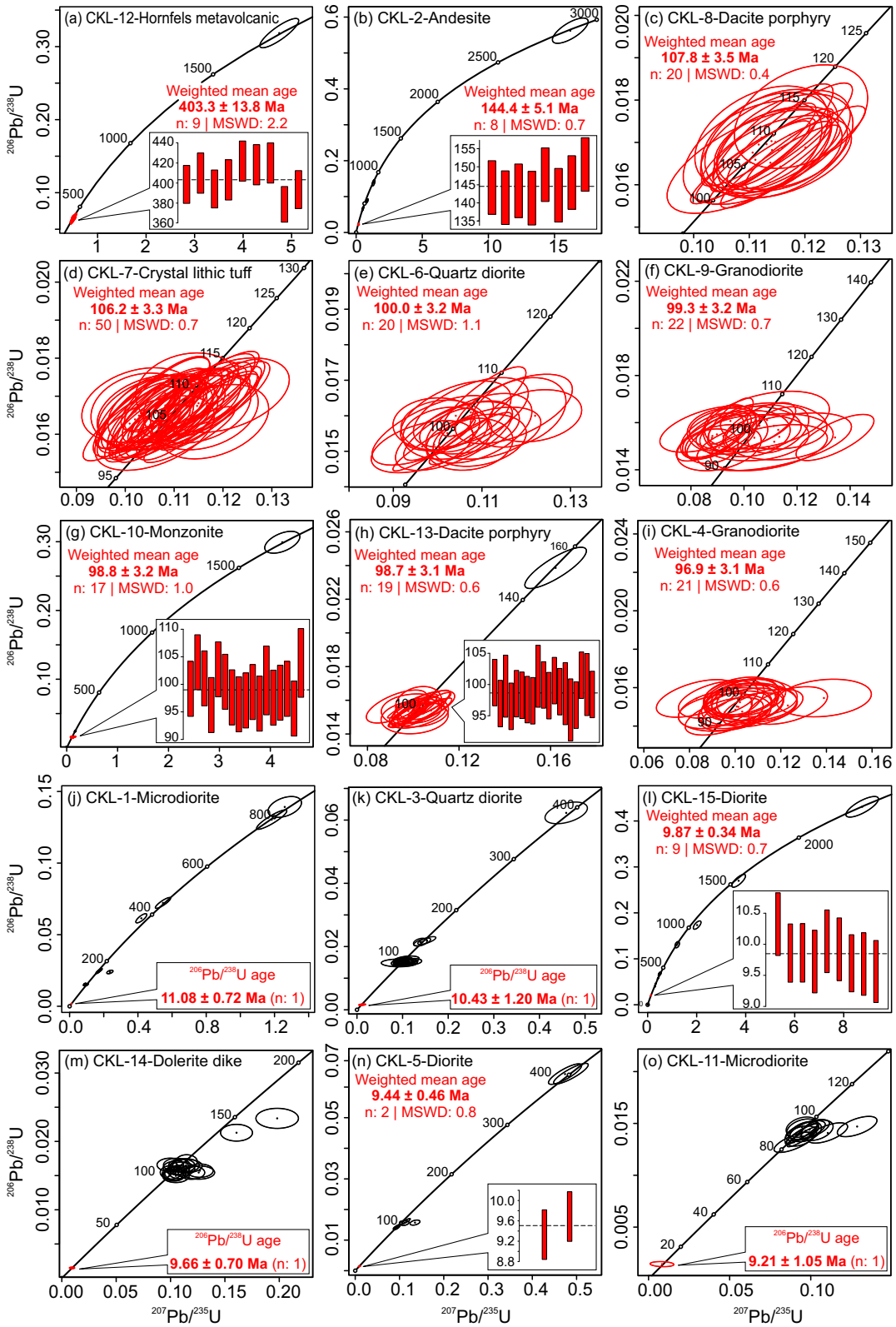

Fig. 13. Zircon U-Pb concordia plots with insets showing the weighted mean $^{206}Pb/^{238}U$ ages (all uncertainties are reported at the 2σ level including σ_{sys}) for metasedimentary basement, intrusive, and volcanic rocks at Ruwai. (a) Devonian hornfels metavolcanic as basement rock. (b-d) Early Cretaceous volcanic rocks. (e-i) Late Cretaceous granitoids and dacite porphyry. (j-o) Late Miocene diorite and dolerite dikes. MSWD = mean square of weighted deviates.

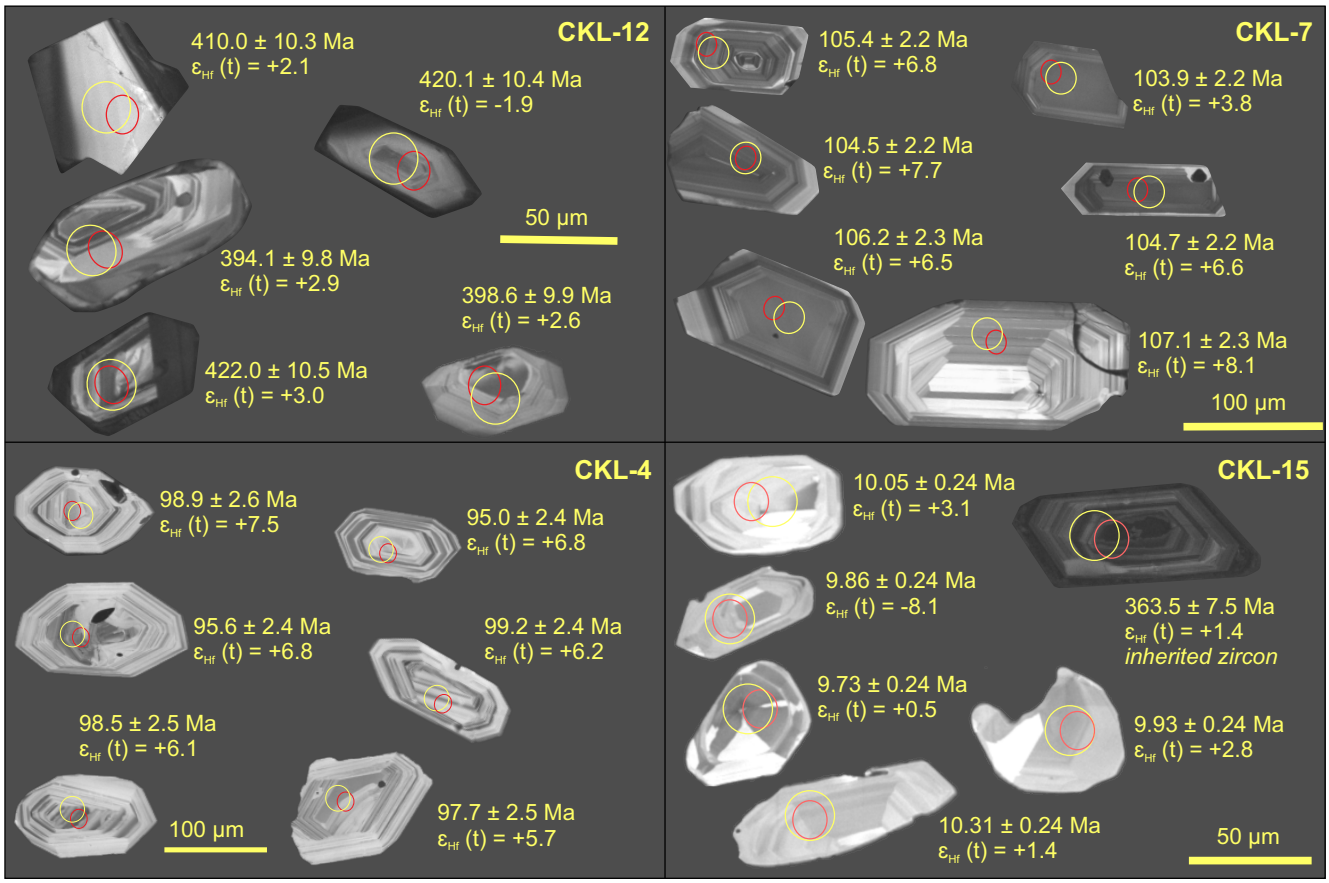

Fig. 14. Representative cathodoluminescence images of zircon from each group of ages (i.e., pre-Cretaceous: CKL-12; Early Cretaceous: CKL-7; Late Cretaceous: CKL-4; and late Miocene: CKL-15). Note: red circle is U-Pb isotope laser point; yellow circle is Hf isotope laser point.

altered dacite porphyry sample yielded similar weighted average $^{206}Pb/^{238}U$ ages to the granitoid samples, i.e., CKL-13: 98.7 ± 1.0 | 31. Ma, n = 19, MSWD = 0.6, $\varepsilon_{Hf_{(t)}}$ = 5.2 to 10.8, with one inherited zircon (152.0 Ma).

Late Miocene (ca. 11.09–9.21 Ma): The youngest magmatism at Ruwai is represented by five dioritic dike samples: CKL-1 (11.08 ± 0.64 | 0.72 Ma, n = 1), CKL-3 (10.43 ± 1.16 | 1.20 Ma, n = 1; $\varepsilon_{Hf_{(t)}}$ = 3.9), CKL-11 (9.21 ± 1.01 | 1.05 Ma, n = 1), CKL-15 (9.87 ± 0.17 | 0.34 Ma, n = 9; MSWD = 0.7), and CKL-5 (9.44 ± 0.36 | 0.46 Ma, n = 2, MSWD = 0.8), as well as one dolerite dike (CKL-14) that cut the orebody and Ketapang Complex limestone wall rocks in the Southwest Gossan open pit (9.66 ± 0.64 | 0.70 Ma, n = 1, $\varepsilon_{Hf_{(t)}}$ = 0.6). The abundance of Cretaceous and Devonian zircons in these Miocene dikes reflects wall-rock contamination from the Kerabai Volcanics, Matan Complex, and syn-ore intrusions. Miocene zircons found in these samples have similar features, including fine to medium grain size, bright CL, and oscillatory zoning patterns (Fig. 14). Most of the Miocene zircons show varying degrees of corrosion; only a few are euhedral and prismatic. The inherited zircons, especially the Paleozoic-Precambrian ones, are characterized by dull CL (Fig. 14).

U-Pb garnet ages

Uranium-lead garnet ages were measured from each garnet type (types I–III; Fig. 15a-c; Table 1). The uncertainty (2σ without | with σ_{sys}) in age estimates is in the range of 1.8 to 4% relative for type I and type II garnet, while for type III it is about 10%. On a Tera-Wasserburg concordia plot (Fig. 15), type I garnet yields a lower intercept U-Pb age of 97.0 ± 1.2 | 1.8 Ma (MSWD = 1.1, n = 117), and type II garnet yields a lower intercept U-Pb age at 95.0 ± 3.6 | 3.9 Ma (MSWD = 0.43, n = 77). Type III overlaps in age with type I and type II garnet with a lower intercept U-Pb age of 94.2 ± 10.2 | 10.3 Ma (MSWD = 0.33, n = 36; Fig. 15; Table 1).

U-Pb titanite ages

Uranium-lead titanite ages were measured from type I and type II titanite (Table 1; Fig. 15d, e). The uncertainty at the 2σ level without and including σ_{sys} in age estimates is less than 3% relative for both types of titanite. Type I titanite yielded a lower intercept U-Pb age of 96.0 ± 2.2 | 2.9 Ma (MSWD = 2.4, n = 24). Type II titanite has an overlapping age with a lower intercept U-Pb age of 95.0 ± 0.8 | 2.0 Ma (MSWD = 1.7, n = 106).

Re-Os Geochronology

Re-Os sulfide ages

Chalcopyrite has the highest Re concentration of the analyzed samples, whereas the lowest Re-Os concentration was in pyrrhotite (Table 2). The $^{187}Re/^{188}Os$ values have a wide range

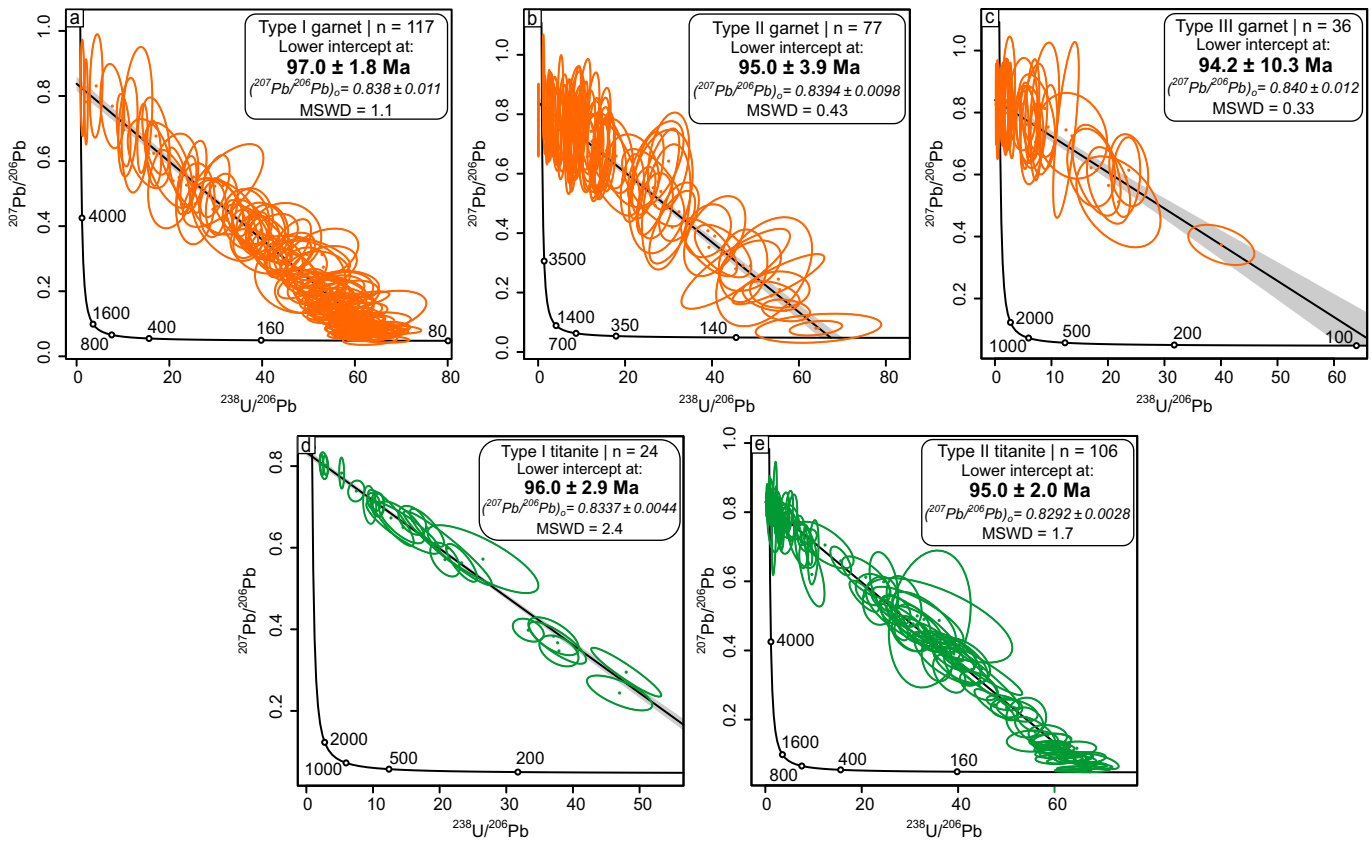

Fig. 15. Concordia plots of garnet (a-c) and titanite (d, e) U-Pb dating are reported at the 2σ level including σ_{sys}. MSWD = mean square of weighted deviates.

from 425 to 61,000, whereas the $^{187}Os/^{188}Os$ values are mostly low and in the range of 2.02 to 7.61, except for two samples of chalcopyrite (20.80) and pyrite (97.6). The $^{187}Os_{radiogenic}$ from these two samples comprises 73.7 and 92.9% of the total Os, respectively. Radiogenic Os concentrations higher than 90% and high $^{187}Re/^{188}Os$ values are diagnostic features of low-level highly radiogenic sulfides (Stein et al., 2000). A maximum likelihood with overdispersion regression (Vermeesch, 2018) of sulfides yields an isochron age of 96.1 ± 2.4 | 2.5 Ma ($^{187}Os/^{188}Os$-dispersion = 0.320 +0.176/–0.094) with an initial $^{187}Os/^{188}Os$ of 1.34 ± 0.19. This age is also consistent with the single model age obtained from that low-level highly radiogenic sulfide, which is 95.0 ± 1.5 Ma. Note that the uncertainties for Re-Os analysis are reported in two standard errors, while uncertainties for the isochron are reported in the 95% confidence interval.

Re-Os magnetite ages

Magnetite grains from four samples were dated by Re-Os, and the results are shown in Table 2. Rhenium concentrations in magnetite range from 0.193 to 44.268 ppb, whereas the Os range from 22.83 to 149.27 ppt. The $^{187}Re/^{188}Os$ values have a wide variation from 7.0 to 3,237.2, whereas the $^{187}Os/^{188}Os$ values range from 1.09 to 6.53. A maximum likelihood with overdispersion regression (Vermeesch, 2018) on these magnetites yielded an isochron age of 99.3 ± 3.6 | 3.7 Ma ($^{187}Os/^{188}Os$-dispersion= 0.082 +0.123/–0.038) with an initial $^{187}Os/^{188}Os$ of 1.07 ± 0.13.

Whole-Rock Geochemistry

The chemical composition and age of the intrusions at Ruwai were compared with data from previous studies (e.g., Widyastanto et al., 2019; Dana et al., 2022a) in the immobile element-based Zr/Ti versus Nb/Y plot (Pearce, 1996; Fig. 16a). Both Cretaceous and Miocene samples from the current study have compositions similar to those of samples described by previous studies (e.g., Widyastanto et al., 2019; Dana et al., 2022a; App. Table A1) with felsic-intermediate samples mainly plotting in the andesite (diorite) and trachyandesite (monzonite) fields, with the exception of one sample that falls into the rhyolite-dacite (granite-granodiorite) field. The mafic sample has a basaltic (gabbro-dolerite) composition, consistent with mafic samples from previous studies. The samples are largely calc-alkaline metaluminous, although a few are peraluminous. The intrusions have low Sr/Y (<40) but high Y (>14.1 ppm) and plot in the normal arc (nonadakitic) volcanic field (Hansen et al., 2002; Fig. 16b, c). On the chondrite-normalized REE plot (McDonough and Sun, 1995; Fig. 16e), most samples (regardless of the age or lithology) have similar elevated LREE/HREE enrichment patterns with negative Eu anomalies. When normalized to the primitive mantle (Sun and McDonough, 1989; Fig. 16f), most samples are enriched in large-ion lithophile elements (LILEs, e.g., K, Rb, and U) and LREEs and have variable degree of depletion of HFSEs (e.g., Hf and Y) and HREEs. The rocks have distinct negative Ba and Nb anomalies (in relationship to Th and U) and positive anomalies in U-Th and Pb (relative to K).

Table 1. Summary of U-Pb Ages from Intrusions, Volcanic Rocks, and Skarn Orebodies

Sample code	Coordinates (UTM) Easting	Coordinates (UTM) Northing	Elevation (m)	Lithology	Mineral analyzed	Average U (ppm)	Average Th (ppm)	Age (Ma)	Uncertainty (2σ) without | with σ_{sys}	MSWD; *N*	$\varepsilon_{Hf_{(t)}}$
CKL-12	532670	9830075	101	Hornfelsed siltstone	Zircon	454.27	317.65	403.3	6.7 | 13.8	2.2; 9	–9.4 to 6.3
CKL-2	533395	9830469	172	Andesite	Zircon	439.91	318.36	144.4	2.7 | 5.1	0.7; 8	–10 to 11.7
CKL-8	531442	9829412	143	Dacite porphyry	Zircon	678.58	516.70	107.8	1.3 | 3.5	0.4; 20	2.4–6.5
CKL-7	530896	9829164	192	Crystal-lithic tuff	Zircon	819.50	864.11	106.2	0.7 | 3.3	0.7; 50	–2.0 to 8.6
CKL-6	534261	9830878	132	Quartz diorite	Zircon	420.64	508.88	100.0	1.0 | 3.2	1.1; 20	4.9–10.3
CKL-9	534403	9830641	212	Granodiorite	Zircon	600.84	762.56	99.3	1.1 | 3.2	0.7; 22	4.1–10.9
CKL-10	534054	9830505	193	Monzonite	Zircon	333.42	476.40	98.8	1.2 | 3.2	1.0; 17	–2.8 to 11.0
CKL-13	532468	9829837	106	Dacite porphyry	Zircon	481.96	1,856.51	98.7	1.0 | 3.1	0.6; 19	5.2–10.8
CKL-4	534685	9830749	144	Granodiorite	Zircon	316.10	322.37	96.9	1.1 | 3.1	0.6; 21	1.2–13.4
CKL-1	533395	9830469	172	Microdiorite	Zircon	719.33	837.97	11.08	0.64 | 0.72	n/a; 1	n/a
CKL-3	534685	9830749	144	Quartz diorite	Zircon	326.41	321.85	10.43	1.16 | 1.20	n/a; 1	4.1–9.9
CKL-15	532842	9830481	155	Diorite	Zircon	800.61	742.87	9.87	0.17 | 0.34	0.7; 9	–12.3 to 9.1
CKL-14	531737	9829438	78	Dolerite	Zircon	429.28	624.79	9.66	0.64 | 0.70	n/a; 1	0.6–12.1
CKL-5	533937	9830886	167	Diorite	Zircon	663.19	1,339.42	9.44	0.36 | 0.46	0.8; 2	–11.1 to 5.2
CKL-11	533253	9830123	179	Microdiorite	Zircon	522.56	810.98	9.21	1.01 | 1.05	n/a; 1	2.6–8.3
CDP-001022	531981	9829689	155	Prograde skarn	Type I garnet	4.66	0.46	97.0	1.2 | 1.8	1.1; 117	n/a
CDP-019023	531880	9829600	135	Prograde skarn	Type II garnet	0.47	1.45	95.0	3.6 | 3.9	0.4; 77	n/a
CDP-000024	531981	9829688	155	Prograde skarn	Type III garnet	2.27	6.59	94.2	10.2 | 10.3	0.3; 36	n/a
CDP-000008	530803	9829126	159	Retrograde skarn	Type I titanite	37.58	193.17	96.0	2.2 | 2.9	2.4; 24	n/a
CDP-000023	531981	9829688	155	Retrograde skarn	Type II titanite	25.78	56.50	95.0	0.8 | 2.0	1.7; 106	n/a

MSWD = mean square of weighted deviates, n/a = not applicable

Table 2. Rhenium-Osmium Concentrations and Their Isotopic Ratios in Sulfides and Magnetite

Sample code	Coordinates (UTM) Easting	Coordinates (UTM) Northing	Elevation (m)	Mineral	Ore type	Re (ppb)	2 SE	Os (ppt)	2 SE	^{187}Os (%)	^{187}Re /^{188}Os	2 SE	^{187}Os /^{188}Os	2 SE
CDP-012	531398	9829380	139	Chalcopyrite	Disseminated	34.09	0.080	50.86	0.25	73.75	11,900	100	20.80	0.20
CDP-009	531066	9829284	152	Pyrite		19.573	0.032	21.19	0.26	92.95	61,000	1,200	97.6	2.2
CDP-010	531066	9829284	152			2.002	0.0008	28.32	0.09	21.45	425	1.5	2.022	0.014
CDP-019	531880	9829600	135			9.802	0.013	58.01	0.08	32.13	1,173	2.5	3.506	0.009
CDP-015	531851	9829605	134		Massive	9.382	0.013	33.104	0.057	36.55	2,102	5.0	4.266	0.012
CDP-010	531066	9829284	152	Pyrrhotite	Disseminated	2.5184	0.0006	13.859	0.040	28.79	1,203	3.8	2.993	0.014
CDP-011	531148	9829343	144			0.37548	0.00022	0.889	0.021	50.70	4,020	160	7.61	0.32
CDP-003a	530570	9829180	146		Massive	4.2534	0.0007	33.19	0.09	24.04	795.8	2.3	2.34	0.010
CDP-003b	530570	9829180	146			3.37058	0.00056	14.012	0.034	39.12	1,859.0	5.5	4.76	0.019
CDP-004	530570	9829180	146			1.39312	0.00042	5.280	0.039	40.95	2,101	18	5.13	0.057
CDP-018	531880	9829600	135			15.0410	0.0052	61.02	0.13	38.44	1,884.2	4.3	4.62	0.015
CDP-011	531148	9829343	144	Sphalerite	Disseminated	2.31971	0.00052	10.62	0.08	32.02	1,514	12	3.49	0.046
CDP-020	532013	9829618	133			2.5649	0.0006	16.42	0.08	31.57	1,076	6	3.42	0.032
CDP-015	531851	9829605	134		Massive	4.3828	0.0009	39.84	0.35	21.73	663	6	2.06	0.035
CDP-018	531880	9829600	135			8.9859	0.0014	78.85	0.10	22.49	693.7	0.9	2.149	0.005
CDP-022	531981	9829689	155	Magnetite	Disseminated	0.19296	0.00050	149.27	0.08	12.80	7.007	0.019	1.087	0.001
CDP-006	530505	9829365	162		Massive	9.7772	0.0013	29.37	0.12	42.26	2,710	14	5.42	0.041
CDP-007	530505	9829365	162			2.3474	0.0006	22.83	0.06	22.26	623.9	1.8	2.12	0.012
CDP-008	530803	9829126	159			44.268	0.012	120.90	0.11	46.86	3,237.2	4.1	6.53	0.012

SE = standard error

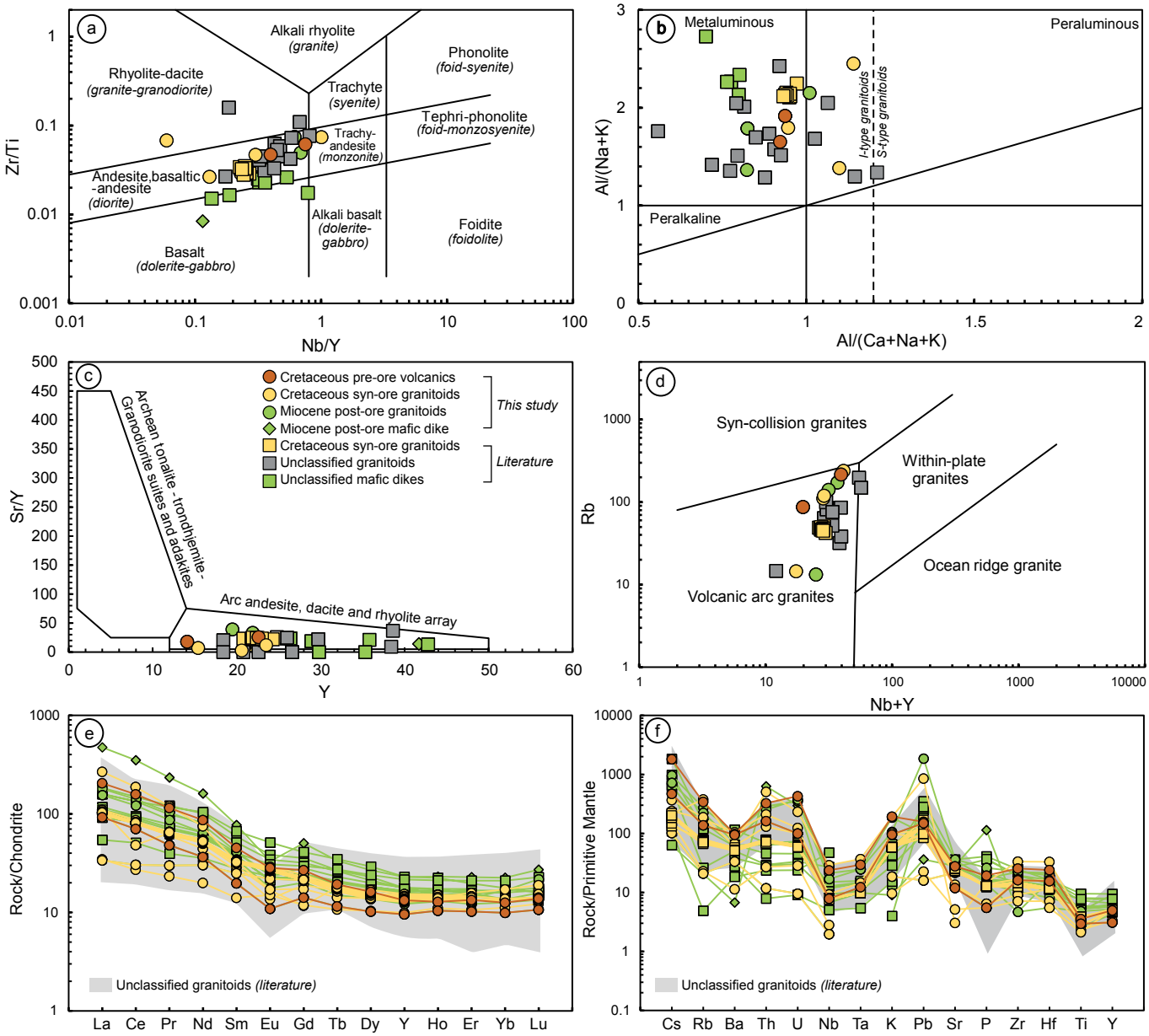

Fig. 16. Geochemical characteristics of intrusions at Ruwai. (a) Nb/Y versus Zr/Ti rock classification (after Pearce, 1996). (b) Alumina saturation index (ASI) diagram (after Maniar and Piccoli, 1989). (c) Y versus Sr/Y diagram (after Hansen et al., 2002). (d) Nb + Y versus Rb tectonic discrimination for granitoid rocks (after Pearce et al., 1984). (e) Chondrite-normalized rare earth element spider diagram (normalization values from McDonough and Sun, 1995). (f) Primitive mantle-normalized multielement spider diagram (normalization values from Sun and McDonough, 1989).

Stable Isotopes

Sulfur isotopes

The sulfur isotope data for sulfides from Ruwai have a wide range of $\delta^{34}S_{V\text{-}CDT}$, from –1.9 to 18.5‰ (Fig. 17; Table 3). The sulfur isotope values of proximal samples are typically lower than distal samples. For instance, pyrite from the proximal area has a $\delta^{34}S_{V\text{-}CDT}$ range of –0.3 to 3.7‰, whereas from the distal part $\delta^{34}S_{V\text{-}CDT}$ is 4.4 to 18.5‰. Similarly, proximal chalcopyrite has $\delta^{34}S_{V\text{-}CDT}$ values of –1.9 to 0.4‰, which increase to 3.4‰ in the distal position. In addition, galena and sphalerite have $\delta^{34}S_{V\text{-}CDT}$ values of 1.2 to 2.9‰ and –0.5 to 2.2‰, respectively, from proximal mineralization, and 2.9 to 3.8‰ and 3.6 to 4.5‰ in the distal part. Distal chalcanthite sample has a $\delta^{34}S_{V\text{-}CDT}$ value of 3.2‰.

Carbon-oxygen isotopes

Calcite carbon and oxygen isotopes were analyzed from marble and from prograde- and retrograde-stage skarn. The carbon and oxygen isotope values decrease gradually from the marble to the retrograde skarn (Fig. 17; Table 4). The $\delta^{13}C_{PDB}$ for marble is –0.7 to 1.4‰ (avg 0.4‰), whereas the values

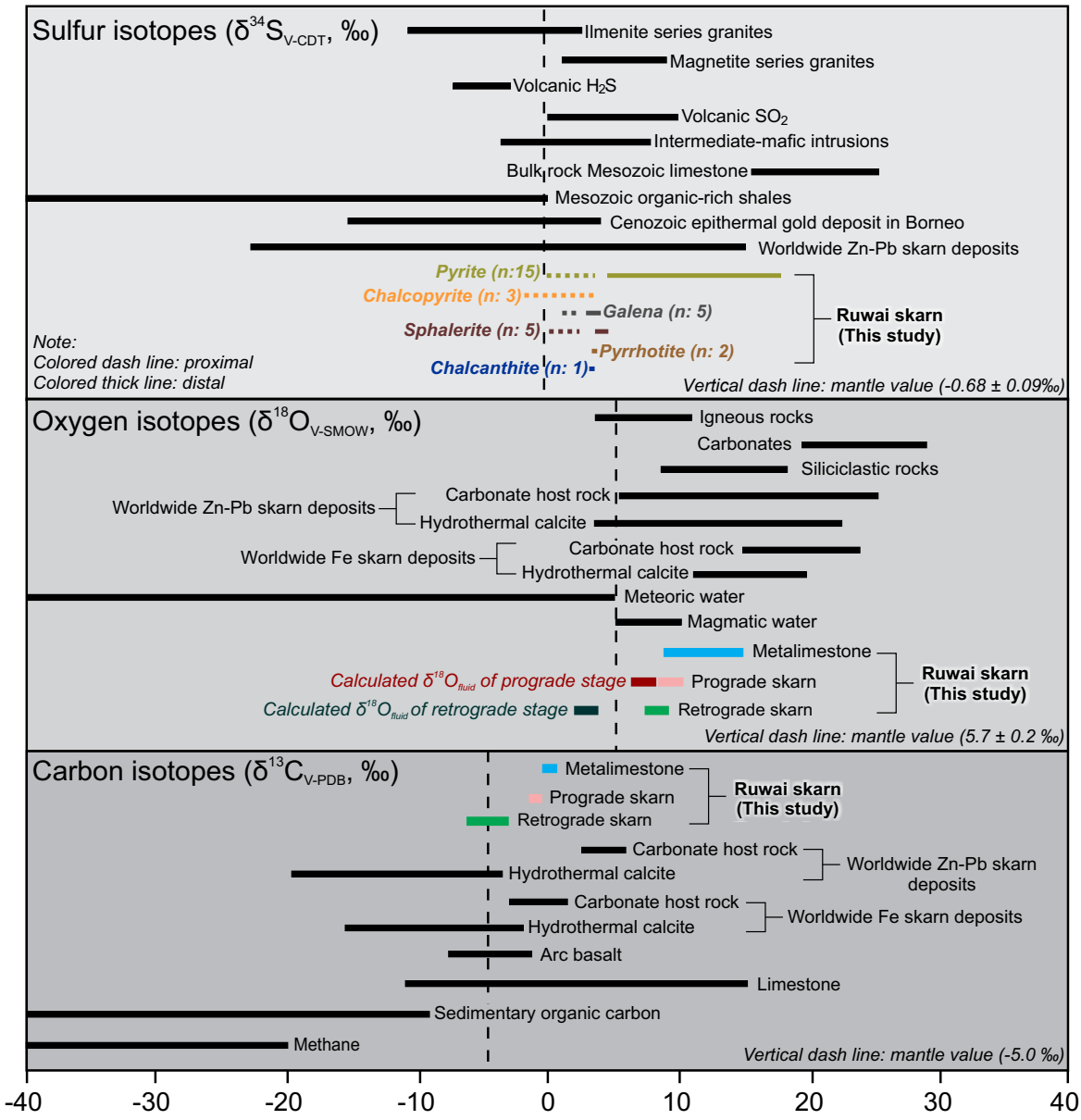

Fig. 17. Carbon-oxygen-sulfur stable isotope variations of Ruwai skarn deposit and several isotopic reservoir references (isotopic data compiled from Seal, 2006; Hoefs, 2015, and references therein). V-CDT = Vienna-Canyon Diablo Troilite, V-PDB = Vienna-Pee Dee Belemnite, V-SMOW = Vienna-standard mean ocean water.

from prograde and retrograde calcite are –1.6 to –1.3‰ (avg –1.5‰) and –6.1 to –3.5‰ (avg –5.1‰), respectively. The average $\delta^{18}O_{PDB}$ for marble is –19.0‰ (ranging from –21.3 to –16.2‰), whereas the values from prograde and retrograde stages are –20.9 (–21.8 to –20.2‰) and 21.63‰ (–22.1 to –20.9‰), respectively. The oxygen isotope composition of hydrothermal fluids in equilibrium with calcite ($\delta^{18}O_{fluid}$) was calculated based on the equation for calcite water of O'Neill and Taylor (1967) assuming temperatures of 511° and 297°C for prograde and retrograde stages, respectively, as inferred from garnet-pyroxene thermometry and chlorite thermometry. The calculated $\delta^{18}O_{fluid}$ in the prograde stage ranges from 7.3 to 9.0‰ and from 3.0 to 4.2‰ in the retrograde stage.

Discussion

Mineralization age and regional metallogenic implications

Determining the age of the mineralization is important for understanding the tectonic setting for ore formation at Ruwai and to potentially guide future exploration (Chelle-Michou et al., 2017; Fu et al., 2018; Waffron et al., 2018; Burisch et al., 2019). Previous workers have considered mineralization in the Central Borneo metallogenic belt to be associated with Cenozoic magmatism (e.g., Garwin, 1997; Setijadji et al., 2010; van Leeuwen, 2018). Our results show that Cretaceous mineralization is also present in the belt, as was first noted at the Late Cretaceous Lamandau Fe-Cu

Table 3. Sulfur Isotope Composition of Sulfides and Sulfate from the Ruwai Skarn Deposit

Sample code	Coordinates (UTM) Easting	Northing	Elevation (m)	Proximity to the intrusion	Ore type	Mineral	$\delta^{34}S_{V\text{-}CDT}$ (‰)
CDP-019	531880	9829600	135	Proximal	Disseminated	Pyrite	3.7
AI-009	531557	9829265	186				–0.3
AI-011	531428	9829341	141				0.9
AI-001	531429	9829341	140				1.0
AI-003	531406	9829386	138				1.1
CDP-012	531398	9829380	139				1.3
CDP-011	531148	9829343	144				2.5
AI-010	531438	9829302	155				2.5
CDP-013	531368	9829462	159				3.4
AI-013	531778	9829479	175	Distal	Massive		4.4
CDP-015	531851	9829605	134				4.9
AI-002	531659	9829551	146				5.2
AI-017	531619	9829433	162				5.5
AI-008	531659	9829551	146				9.8
AI-015	531678	9829508	154				18.5
AI-014	531480	9829355	147	Proximal	Disseminated	Chalcopyrite	–1.9
AI-012	531503	9829378	144				–0.4
CDP-012	531398	9829380	139				3.4
CDP-012	531398	9829380	139	Proximal	Disseminated	Galena	1.2
CDP-011	531148	9829343	144				2.0
CDP-013	531368	9829462	159				2.6
CDP-018	531880	9829600	135	Distal	Massive		2.9
CDP-015	531851	9829605	134				3.8
CDP-003	530570	9829180	146	Distal	Massive	Pyrrhotite	3.5
CDP-018	531880	9829600	135				3.5
AI-009	531557	9829265	186	Proximal	Disseminated	Sphalerite	–0.5
CDP-012	531398	9829380	139				0.4
CDP-011	531148	9829343	144				2.2
CDP-018	531880	9829600	135	Distal	Massive		3.6
CDP-015	531851	9829605	134				4.5
CDP-025	531815	9829350	153		Not defined	Chalcanthite	3.2

V-CDT = Vienna-Canyon Diablo Troilite

Table 4. Carbon and Oxygen Isotope Compositions of Calcite from the Ruwai Skarn Deposit

Sample code	Rock type	Coordinates (UTM) Easting	Northing	Elevation (m)	Proximity to the intrusion	Measured $\delta^{13}C_{PDB}$ (‰)	Measured $\delta^{18}O_{PDB}$ (‰)	Calculated $\delta^{18}O_{V\text{-}SMOW}$ (‰)	Calculated $\delta^{18}O_{Fluid}$ (‰)
CDP-005A	Marble	530505	9829365	162	Distal	–0.7	–20.9	9.4	n.a.
CDP-016A		531851	9829605	134		1.4	–20.8	9.5	
CDP-020A		532013	9829618	133		0.1	–16.2	14.3	
CDP-301		531561	9829405	155	Proximal	1.2	–17.7	12.7	
CDP-307		531532	9829324	161		0.5	–21.3	8.9	
CDP-308		531360	9829348	143		–0.4	–17.2	13.2	
CDP-019	Prograde	531880	9829600	135	Proximal	–1.3	–21.8	8.5	7.3
CDP-022	skarn	531981	9829689	155	Distal	–1.6	–20.8	9.5	8.4
CDP-023		531981	9829688	155		–1.5	–20.2	10.1	9.0
CDP-009	Retrograde	531066	9829284	152	Proximal	–5.2	–21.5	8.7	3.5
CDP-013	skarn	531368	9829462	159		–6.1	–21.9	8.4	3.2
CDP-014		531368	9829462	159		–6.0	–21.8	8.5	3.3
CDP-014A		531368	9829462	159		–4.4	–21.6	8.6	3.5
CDP-007		530505	9829365	162	Distal	–3.5	–22.1	8.1	3.0
CDP-020		532013	9829618	133		–5.3	–20.9	9.4	4.2

Note: The $\delta^{18}O_{Fluid}$ is calculated based on formula from O'Neill and Taylor (1967)
Abbreviations: n.a. = not analyzed, PDB = Pee Dee Belemnite, V-SMOW = Vienna-standard mean ocean water

deposit (Fig. 18; Li et al., 2015). At Ruwai, garnet, titanite, magnetite, and sulfides yielded Late Cretaceous ages (ca. 99.3–94.2 Ma; Figs. 15, 19), which is consistent with our U-Pb zircon ages of associated intrusive bodies. Magmatism at Ruwai generally can be divided into three phases: (1) Early Cretaceous (pre-ore), (2) Late Cretaceous (syn-ore), and (3) Miocene (post-ore; Figs. 13, 18). Although broadly similar, the three magmatic phases have some geochemical and isotopic differences. Syn-ore intrusions have relatively low total LILEs (avg 750 ppm), HFSEs (avg 238 ppm), and REEs (avg 131 ppm) contents compared to pre-ore (LILEs: avg 1,263 ppm; HFSEs: avg 296 ppm; REEs: avg 161 ppm) and post-ore (LILEs: avg 1,105 ppm; HFSEs: avg 249 ppm; REEs: avg 200 ppm). The ε_{Hf} isotopic compositions are mostly positive and decrease from pre- to post-ore stages (Fig. 20a, b), consistent with melting of crustal material (which was derived from the depleted mantle) during the Mesoproterozoic to Neoproterozoic. Minor zircon grains with either low ε_{Hf} values or Neo- to Mesoproterozoic age indicate reworking of older crust, possibly of Paleoproterozoic and Neoarchean

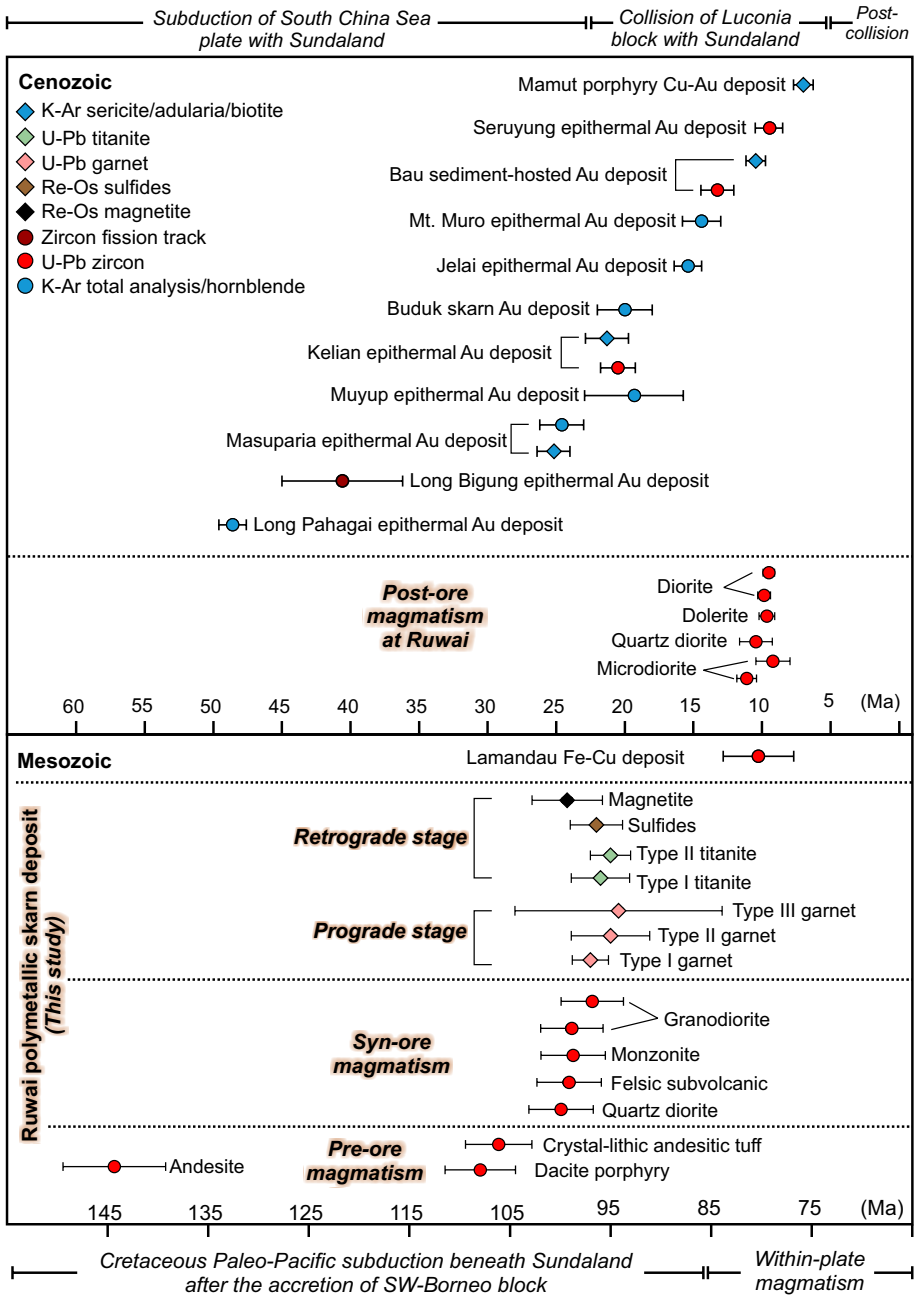

Fig. 18. Regional geochronology of igneous rocks and mineral deposits in Borneo (data compiled from Thompson et al., 1994; Imai, 2000; Davies et al., 2008; Baharuddin, 2011; Li et al., 2015; Percival et al., 2018; Breitfeld et al., 2019; Lai et al., 2021). The Ruwai skarn deposit formed during the Cretaceous along with the Lamandau Fe-Cu deposit, whereas epithermal gold mineralization was associated with Oligo-Miocene magmatism. Note: the uncertainties are reported at 2σ level.

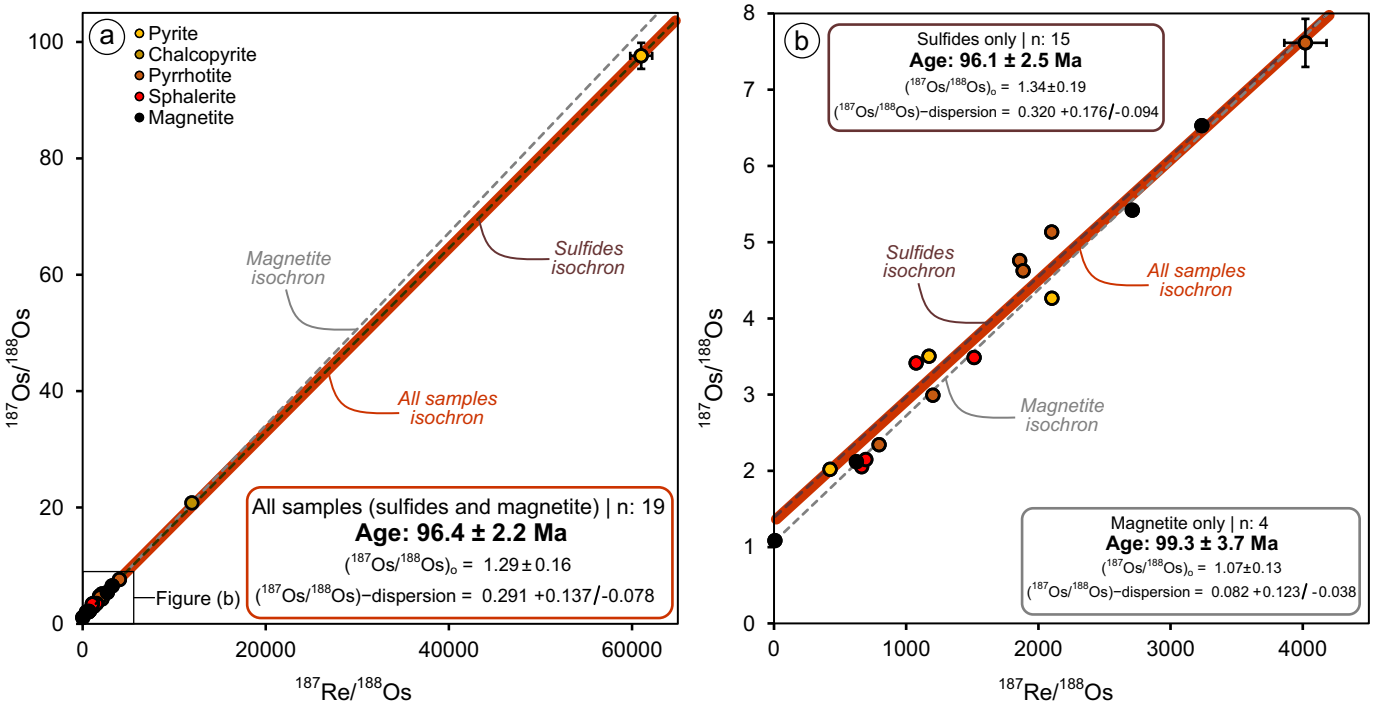

Fig. 19. Isochron plots of $^{187}Re/^{188}Os$ versus $^{187}Os/^{188}Os$ for sulfides and magnetite from the Ruwai skarn deposit (all uncertainties are reported at the 2σ level including σ_{sys}).

age. Three prograde garnet types yielded U-Pb ages of 97.0 ± 1.8, 95.0 ± 3.9, and 94.2 ± 10.3 Ma, respectively. These ages overlap with the U-Pb ages of retrograde-stage titanite, i.e., 96.0 ± 2.9 and 95.0 ± 2.0 Ma. Rhenium-Os ages of the retrograde-stage sulfides and magnetite are 96.0 ± 2.3 and 99.3 ± 3.6 Ma, respectively.

Cretaceous magmatism at Ruwai was likely associated with Paleo-Pacific subduction after the accretion of the Southwest Borneo block to Sundaland (e.g., Davies et al., 2014; Hennig et al., 2017). Miocene magmatism was associated with the subduction of the South China Sea plate, followed by the collision of the Luconia block with Sundaland (Soeria-Atmadja et al., 1999). The chemical compositions of Cretaceous and Miocene magmatic rocks at Ruwai are consistent with a volcanic-arc origin (Fig. 16d). Early Cretaceous magmatism produced the andesitic-dacitic Kerabai Volcanics, whereas Miocene magmatism was dominated by the dioritic Sintang Suite. Late Cretaceous magmatism evolved to more felsic (i.e., quartz diorite, monzonite, and granodiorite) with time, with the more evolved magma associated with skarn mineralization at Ruwai. Although the regional geologic map attributes the granitoids around Ruwai to the Sukadana granite (Margono et al., 1995), Breitfeld et al. (2020) showed that this granitoid is younger (ca. 80 Ma) than the granitoids at Ruwai, as also shown in our results (ca. 99.7–97.1 Ma). Breitfeld at al. (2020) also demonstrated that the Sukadana granitoids were associated with within-plate magmatism, whereas mineralization at Ruwai is subduction related (Fig. 16d). We therefore propose that the granitoids at Ruwai represent an older suite of Sukadana granitoids that formed at the end of subduction, before the start of within-plate magmatism, as proposed by Breitfeld et al. (2020).

Physicochemical conditions of skarn mineralization at Ruwai

Prograde and retrograde temperature: Temperatures are constrained by mineral and sulfur isotope geothermometry (Table 5). The temperature of the prograde stage (401°–673° ± 66°C, avg 511°C) was estimated based on the garnet-clinopyroxene geothermometer of Powell (1985). These temperatures are consistent with other prograde stages (Meinert, 1992; Meinert et al., 2005). On average, the temperature estimates decrease from type I to type III garnet (type I: 406°–673°C; type II: 401°–646°C; type III: 414°–543°C). The temperatures of the retrograde stage have been estimated using the chlorite thermometer of Hillier and Velde (1991) and are around 195° to 377° ± 56°C (avg 297°C). These temperature ranges are consistent with the results from a previous fluid inclusion study that suggested retrograde temperatures of 190° to 260°C (Idrus et al., 2011). Although slightly lower than those obtained from chlorite geothermometry (195°–377°C) and fluid inclusion microthermometry (190°–260°C; Idrus et al., 2011), the temperature from pyrite-chalcopyrite pairs (162°–217° ± 40°C) is similar to the late retrograde-stage temperature and likely indicative of the true equilibration temperature. The temperatures from galena-pyrrhotite pairs (410°–460° ± 25°C) are consistent with the temperature estimated from arsenopyrite geothermometry (428°–493°C; Dana et al., 2022b). The results from pyrite-sphalerite pairs (264°–349° ± 55°C), are consistent with those results, although they slightly higher than those obtained from the pyrite-chalcopyrite pair in the same sample.

Redox evolution: Early formed garnets have high andradite contents and strong positive Eu anomalies, whereas Eu anom-

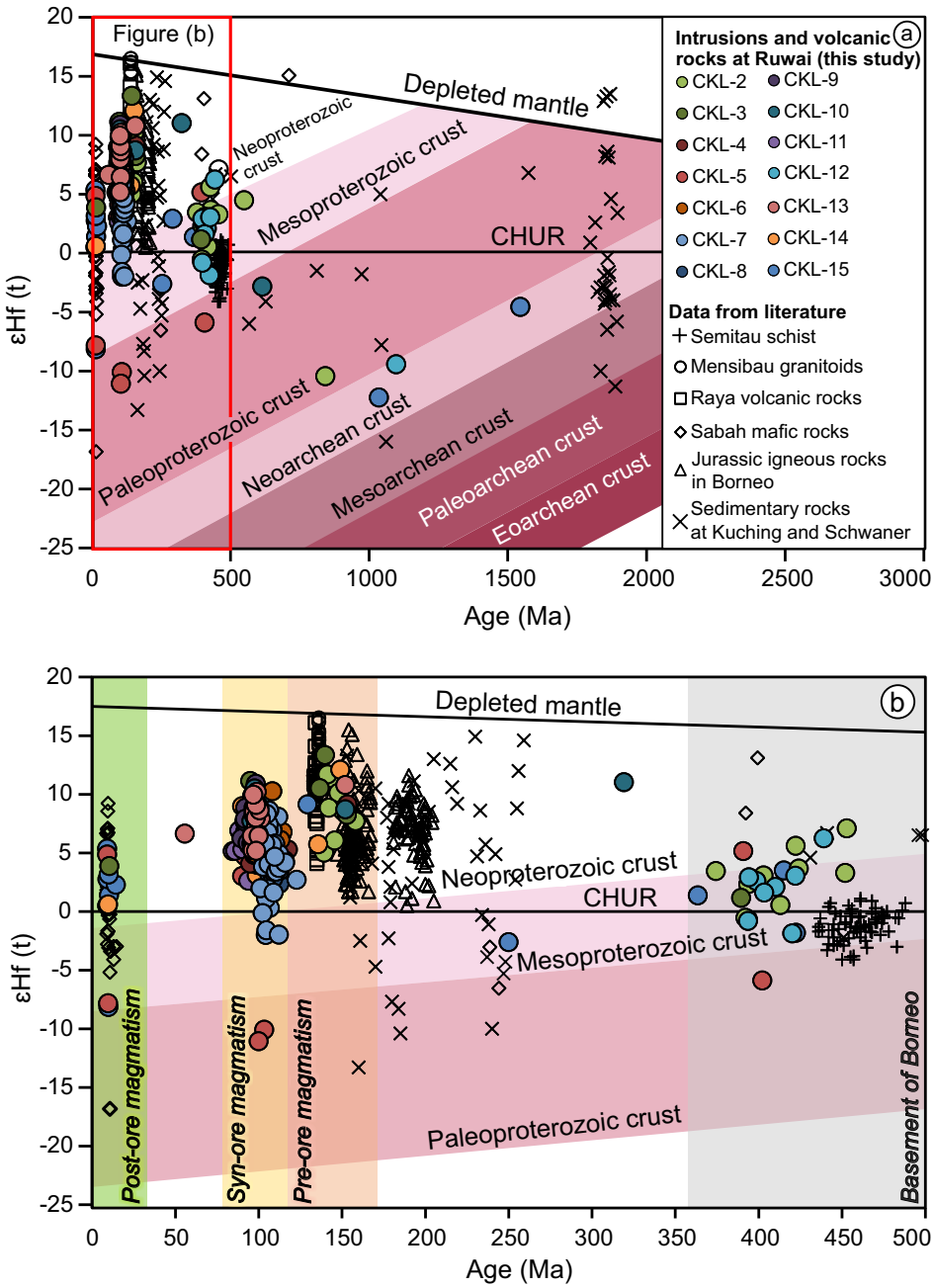

Fig. 20. (a, b) Plots of epsilon hafnium values of zircon against the U-Pb ages for the basement rock and pre-ore, syn-ore, and post-ore intrusions at Ruwai (diagram modified after Kostrovitsky et al., 2016; hafnium isotope data of Semitau schist from Zhu et al., 2022; Raya volcanic rocks and Mensibau granitoids from Wang et al., 2022b; Sabah mafic rocks from Tsikouras et al., 2021; Jurassic igneous and sedimentary rocks at Kuching and Schwaner from Wang et al., 2022a). CHUR = chondritic uniform reservoir.

alies are negative or absent, and andradite contents are lower in later garnet (Fig. 9), consistent with decreasing f_{O_2} with time in the prograde stage (Jamtveit et al., 1993; Crowe et al., 2001; Smith et al., 2004). Narrow andradite bands, which have positive Eu anomalies in type II garnet (Fig. 8b), however, suggest a transient increase of f_{O_2} from the early to prograde stage within an overall decreasing trend. The mode of occurrence, as well as the chemical composition, of titanite in this study indicates a hydrothermal origin (e.g., REE content, Fe/Al), and it can be used to monitor the redox conditions in the hydrothermal fluids (Horie et al., 2008; Song et al., 2019). At Ruwai, a strong negative Eu anomaly characterizes type I titanite, whereas type II titanite mostly lacks this negative Eu anomaly (Fig. 10d, e), implying that oxidized conditions prevailed during the retrograde stage. This is consistent with the retrograde overgrowth of Al epidote by Fe epidote (Fig. 11e, f) and the replacement of pyrite by magnetite (Fig. 6f) and of magnetite by hematite (Fig. 6b). The extensive formation of

Table 5. Estimated Ore-Forming Temperature of the Ruwai Deposit Based on Multiple Mineral Geothermometry

Thermometry		Stage	Temperature[1] (°C)	Formula	References
Garnet-pyroxene geothermometry	Type I garnet	Prograde	406–673 (±66)	Powell (1985)	This study
	Type II garnet		401–646 (±66)		
	Type III garnet		414–543 (±66)		
Chlorite geothermometry		Retrograde	195-377 (±56)	Hillier and Velde (1991)	
Sulfur isotope geothermometry	Pyrite-chalcopyrite pair		162–217 (±40)	Ohmoto and Rye (1979)	
	Galena-pyrrhotite pair		410–460 (±25)		
	Pyrite-sphalerite pair		264–349 (±55)		
Sphalerite geothermometry	Low Fe sphalerite		245–315 (±18)	Keith et al. (2014)	Idrus et al. (2023)
	High Fe sphalerite		316–432 (±32)		
Arsenopyrite geothermometry	Arsenopyrite-pyrite-pyrrhotite assemblages		428–493	Kretschmar and Scott (1976)	Dana et al. (2022b)
Fluid inclusions on quartz and calcite			190–260	Not applicable	Idrus et al. (2011)

[1]Accuracy for garnet-pyroxene, chlorite, and sphalerite geothermometry represents the standard deviation of mean value (1 SD), while that for sulfur isotope geothermometry represents the uncertainty caused by the analytical error in $\delta^{34}S$ of ± 0.2‰

pyrrhotite after pyrite (Fig. 6c, f) suggests that the sulfidation state decreased in the retrograde stage.

Source of ore-forming fluids and metals

Source of sulfur: Lead-zinc skarn deposits tend to have wide ranges of $\delta^{34}S$ values (Fig. 17), suggesting that the sulfur is likely derived from various sources (e.g., Palinkas et al., 2013; Gao et al., 2020). Sulfur in skarn deposits commences from a magmatic source, with a component of sedimentary-derived sulfur acquired in distal zones (e.g., Megaw et al., 1988; Meinert et al., 2005). At Ruwai, proximal disseminated sulfide ores have lower $\delta^{34}S$ (–1.9 to 3.4‰), whereas distal massive ores have higher $\delta^{34}S$ values (2.9–18.6‰). Sphalerite, galena, and pyrite in the disseminated ores have lower $\delta^{34}S$ (sphalerite: –0.5 to 2.2‰; galena: 1.2–2.6‰; pyrite: –0.3 to 3.4‰) than those from massive ores (sphalerite: 3.6–4.5‰; galena: 2.9–3.8‰; pyrite: 4.4–18.5‰). This increase in $\delta^{34}S$ values from proximal to distal zones could indicate mixing of two sulfur sources or transition from oxidizing to reducing conditions (Wilson et al., 2007). Alternatively, a contribution of seawater-derived sulfate from marble host rock could explain the elevated $\delta^{34}S$ values (Choi et al., 2018; Zhong et al., 2018).

Source of carbon and oxygen: Magmatic hydrothermal fluids play an important role in the skarn formation, particularly during the prograde stage (Einaudi et al., 2003; Meinert et al., 2005). Meteoric water can play a significant role during the retrograde stage (Meinert et al., 2003; Baker et al., 2004). Generally, hydrothermal calcite from Fe and Pb-Zn skarns has a wider $\delta^{13}C$ range with more negative values compared to other skarn types (e.g., Demir and Disli, 2020; Im et al., 2020). Lead-zinc skarns typically have wider $\delta^{18}O$ ranges than other skarn types, both in the carbonate host rock and in the hydrothermal calcite (e.g., Shimazaki and Kusakabe, 1990; Vazquez et al., 1998; Jansson et al., 2021). At Ruwai, the $\delta^{13}C$ and $\delta^{18}O$ values of calcite decrease from the marble host rock to the skarn (Fig. 17). The $\delta^{13}C$ and $\delta^{18}O$ values in the prograde stage are similar to those from the marble host rock (Fig. 17), clearly suggesting that both carbon and oxygen in the prograde calcite were derived from calcite of the marble through carbonate dissolution and/or incomplete replacement.

Source of metals: Calculated initial $^{187}Os/^{188}Os$ values from sulfides (1.34 ± 0.19; n = 15) and magnetite (1.07 ± 0.13; n = 4; Table 2) consistently show much higher values than the mantle (0.11–0.15; Shirey and Walker, 1998), indicating significant contribution of ore-forming metals from the crust (Peucker-Ehrenbrink and Jahn, 2001). Granitoid intrusions around the Schwaner mountains, where the deposit is located, are interpreted to have formed by partial melting of the mantle wedge with some input of crustal material or recycled sediments based on multiple isotopic signatures (Sr-Nd-Pb-Hf-O; Breitfeld et al., 2020; Wang et al., 2022a, b). At Ruwai, zircon Hf isotope compositions (Table 1; Fig. 20) imply that the causative intrusions have a juvenile mantle origin with minor crustal inheritance (Fig. 20a, b). The dominantly crustal initial Os isotope signature of sulfides and magnetite (Table 2; Fig 19) from Ruwai suggests that the ore-forming fluids substantially reacted with a high Re and/or Os unit, possibly the Kuayan Formation or Ketapang Complex, before depositing ore minerals.

Conclusions

The Ruwai skarn deposit formed in the Late Cretaceous (ca. 99.3–94.2 Ma) during the emplacement of Sukadana granite, as subduction of the Paleo-Pacific plate under Sundaland ceased. Magmatism at Ruwai occurred in three phases: Early Cretaceous (ca. 145.7–105.7 Ma; pre-ore), Late Cretaceous (ca. 99.7–97.1 Ma; syn-ore), and Miocene (ca. 10.94–9.51 Ma; post-ore). The Ruwai skarn deposit formed from oxidized and weakly acidic to near-neutral pH hydrothermal fluids of magmatic origin together with a meteoric water fluid component during the retrograde stage.

Our geochronological data also confirmed that the Cretaceous suites within the Central Borneo metallogenic belt are fertile for mineralization, which further opens the opportunity to explore other Mesozoic suites. Yet, more geochronological studies are necessary to confirm the age of gold and

base metal mineralization in other deposits across the Central Borneo metallogenic belt.

Acknowledgments

This research was part of an M.Sc. study by the first author that was funded by Japanese Government (MEXT) Scholarship 2019/2022; the first author is currently a Ph.D. student at the University of Edinburgh, supported by a National Environment Research Council (NERC) Doctoral Training Partnership grant (NE/S007407/1). The Re-Os analysis was financially supported by the Japan Society for the Promotion of Science (JSPS) KAKENHI grants JP20J22038 to M. Ishida, 20K22333 to M. Yano, 19K14817 and 21K14011 to J. Ohta, and 20H05658 to Y. Kato. The whole-rock geochemical and zircon U-Pb-Hf analyses were funded by the international collaborative Borneo Gold Deposit Project (Universiti Brunei Darussalam; UBD) awarded to C.K. Lai. We would like to thank Jochen Kolb of Karlsruhe Institute of Technology for his technical assistance to the third coauthor with in situ sulfur isotope analysis. Special thanks go to Franz Meyer and Roman Klinghardt of RWTH Aachen University and Renaldi Suhendra of Akita University for the assistance during EPMA analysis. We also extend our gratitude to Hinako Sato and Pearlyn Manalo of Akita University for the support during additional sulfur isotope analyses. The authors would like also to acknowledge the management and geologists of PT Kapuas Prima Coal, Tbk., for permission to access the site, support during field work, and financial support for sample shipment from Indonesia to Japan. Constructive comments from the reviewers, Stephanie Mrozek and Jay Thompson, as well as from the associate editor, David Cooke, are greatly appreciated.

REFERENCES

Abidin, H.Z., 1996, The tectonic history and mineral deposits of the east-central Kalimantan volcanic belt, Indonesia: A comparative study of the Kelian, Muyup and Masupa Ria gold deposits: Unpublished Ph.D. thesis, Adelaide, Australia, The University of Adelaide, 286 p.

Advokaat, E.L., Marshall, N.T., Li, S., Spakman, W., Krijgsman, W., and van Hinsbergen, D.J.J., 2018, Cenozoic rotation history of Borneo and Sundaland, SE Asia revealed by paleomagnetism, seismic tomography, and kinematic reconstruction: Tectonics, v. 37, p. 2486–2512, doi: 10.1029/2018TC005010.

Aleinikoff, R.P., Wintsch, R.P., Tollo, R.P., Unruh, D.M., Fanning, C.M., and Schmitz, M.D., 2007, Ages and origins of rocks of the Killingworth dome, south-central Connecticut: Implications for the tectonic evolution of southern New England: American Journal of Science, v. 307, p. 63–118, doi: 10.2475/01.2007.04.

Baharuddin, B., 2011, Petrologi dan geokimia batuan gunungapi Tersier Jelai di daerah Malinau Kalimantan Timur: Jurnal Sumber Daya Geologi, v. 21, p. 203–211.

Baker, T., van Achterberg, E., Ryan, C.G., and Lang, J.R., 2004, Composition and evolution of ore fluids in a magmatic-hydrothermal skarn deposit: Geology, v. 32, p. 117–120, doi: 10.1130/G19950.1.

Basir, J., and Uyop, S., 1999, Significance of Early Jurassic radiolaria from West Sarawak, Malaysia: Regional Congress on Geology, Mineral and Energy Resources of Southeast Asia, 9th, Kuala Lumpur, Malaysia, August 17–19, 1998, Proceedings, p. 491–502.

Breitfeld, H.T., Hall, R., Galin, T., Forster, M.A., and BouDagher-Fadel, M.K., 2017, A Triassic to Cretaceous Sundaland-Pacific subduction margin in West Sarawak, Borneo: Tectonophysics, v. 694, p. 35–56, doi: 10.1016/j.tecto.2016.11.034.

Breitfeld, H.T., Macpherson, C., Hall, R., Thirlwall, M., Ottley, C.J., and Hennig-Breitfeld, J., 2019, Adakites without a slab: Remelting of hydrous basalt in the crust and shallow mantle of Borneo to produce the Miocene Sintang Suite and Bau Suite magmatism of West Sarawak: Lithos, v. 344–345, p. 100–121, doi: 10.1016/j.lithos.2019.06.016.

Breitfeld, H.T., Davies, L., Hall, R., Armstrong, R., Forster, M., Lister, G., Thirlwall, M., Grassineau, N., Hennig-Breitfeld, J., and van Hattum, M.W.A., 2020, Mesozoic Paleo-Pacific subduction beneath SW Borneo: U-Pb geochronology of the Schwaner granitoids and the Pinoh Metamorphic Group: Frontiers in Earth Science, v. 8, article 568715, doi: 10.3389/feart.2020.568715.

Burisch, M., Gerdes, A., Meinert, L.D., Albert, R., Seifert, T., and Gutzmer, J., 2019, The essence of time—fertile skarn formation in the Variscan orogenic belt: Earth and Planetary Science Letters, v. 519, p. 165–170, doi: 10.1016/j.epsl.2019.05.015.

Butler, R.F., Gehrels, G.E., Baldwin, S.L., and Davidson, C., 2002, Paleomagnetism and geochronology of the Ecstall pluton in the Coast Mountains of British Columbia: Evidence for local deformation rather than large-scale transport: Journal of Geophysical Research, v. 107 (B1), doi: 10.1029/2001JB000270.

Chelle-Michou, C., Rottier, B., Caricchi, L., and Simpson, G., 2017, Tempo of magma degassing and the genesis of porphyry copper deposits: Scientific Reports, v. 7, article 40566, doi: 10.1038/srep40566.

Choi, J., Shin, D., and Im, H., 2018, Regional variations of sulfur isotope compositions for metallic deposits in the Taebaeksan mineralized district, South Korea: Geosciences Journal, v. 22, p. 79–89, doi: 10.1007/s12303-017-0057-x.

Coggon, J.A., Nowell, G.M., Pearson, D.G., LLorand, J.-P., Oberthür, T., and Parman, S.W., 2010, Dating platinum mineralisation using the ^{190}Pt-^{186}Os system: Examples from the Bushveld Complex, RSA and the Meratus ophiolite, Borneo: International Platinum Symposium, 11th, Ontario, Canada, June 21–24, 2010, Extended Abstracts, p. 1–4.

Crowe, D.E., Riciputi, L.R., Bezenek, S., and Ignatiev, A., 2001, Oxygen isotope and trace element zoning in hydrothermal garnets: Windows into large-scale fluid-flow behavior: Geology, v. 29, p. 479–482, doi: 10.1130/0091-7613(2001)029<0479:OIATEZ>2.0.CO;2.

Dana, C.D.P., Simarmata, J.R., Aditya, P.G.S., and Widyastanto, A., 2019, Hydrothermal alteration zoning and mineralization style in Southwest Gossan block of Ruwai skarn Zn-Pb-Ag deposit, Lamandau, Central Borneo: An implication to ore genesis and exploration: Himpunan Ahli Geofisika Indonesia (Indonesian Association of Geophysicists)-Ikatan Ahli Geologi Indonesia (Indonesian Association of Geologists)-Ikatan Ahli Fasilitas Produksi Minyak dan Gas Bumi Indonesia (Indonesian Association of Production Facilities for Oil and Gas)-Ikatan Ahli Teknik Perminyakan Indonesia (Indonesian Association of Petroleum Engineers), (HAGI-IAGI-IAFMI-IATMI), Joint Convention, Yogyakarta, Indonesia, November 25–29, 2019, Proceedings, p. 1–6.

Dana, C.D.P., Agangi, A., Takahashi, R., Idrus, A., Lai, C.-K., and Nainggolan, N.A., 2022a, Element mobility during formation of the Ruwai Zn-Pb-Ag skarn deposit, Central Borneo, Indonesia: Resource Geology, v. 72, article e12290, doi: 10.1111/rge.12290.

Dana, C.D.P., Agangi, A., Idrus, A., Lai, C.-K., and Simbolon, D.R., 2022b, Bi-Ag-sulfosalts and sulfoarsenides in the Ruwai Zn-Pb-Ag skarn deposit, Central Borneo, Indonesia: Minerals, v. 12, article 1564, doi: 10.3390/min12121564.

Davies, A.G.S., 2002, Geology and genesis of the Kelian gold deposit, East Kalimantan, Indonesia: Unpublished Ph.D. thesis, Tasmania, Australia, University of Tasmania, 404 p.

Davies, A.G.S., Cooke, D.R., Gemmell, J.B., and Simpson, K.A., 2008, Diatreme breccias at the Kelian gold mine, Kalimantan, Indonesia: Precursors to epithermal gold mineralization: Economic Geology, v. 103, p. 689–716, doi: 10.2113/gsecongeo.103.4.689.

Davies, L., Hall, R., and Armstrong, R., 2014, Cretaceous crust in SW Borneo: Petrological, geochemical and geochronological constraints from the Schwaner mountains: Indonesian Petroleum Association Annual Convention and Exhibition, 38th, Jakarta, Indonesia, May 21–23, 2014, Proceedings, p. 1–15.

De Keyser, F., and Rustandi, E., 1993, Geology of the Ketapang sheet area, Kalimantan, Bandung, Indonesia: Bandung, Indonesia, Geological Research and Development Centre, scale 1:250,000.

Demir, Y., and Dişli, A., 2020, Fluid inclusion and stable isotope constraints (C, O, H) on the Dağbaşı Fe-Cu-Zn skarn mineralization (Trabzon, NE Turkey): Ore Geology Reviews, v. 116, article 103235, doi: 10.1016/j.oregeorev.2019.103235.

Deng, X.D., Li, J.W., Luo, T., and Wang H.Q., 2017, Dating magmatic and hydrothermal processes using andradite-rich garnet U-Pb geochronometry:

Contributions to Mineralogy and Petrology, v. 172, article 71, doi: 10.1007/s00410-017-1389-2.
Droop, G.T.R., 1987, A general equation for estimating Fe^{3+} concentrations in ferromagnesian silicates and oxides from microprobe analyses, using stoichiometric criteria: Mineralogical Magazine, v. 51, p. 431–435, doi: 10.1180/minmag.1987.051.361.10.
Einaudi, M.T., Hedenquist, J.W., and Inan, E.E., 2003, Sulfidation state of fluids in active and extinct hydrothermal systems: Transitions from porphyry to epithermal environments: Society of Economic Geologists, Special Publication 10, p. 285–313, doi: 10.5382/SP.10.15.
Franz, G., and Liebscher, A., 2004, Physical and chemical properties of the epidote minerals: An introduction: Reviews in Mineralogy and Geochemistry, v. 56, p. 1–81, doi: 10.2138/gsrmg.56.1.1.
Fu, Y., Sun, X., Li, D., and Lin, H., 2018, U-Pb geochronology and geochemistry of U-rich garnet from the giant Beiya gold-polymetallic deposit in SW China: Constraints on skarn mineralization process: Minerals, v. 8, p. 1–19, doi: 10.3390/min8040128.
Gao, B., Li, W., Jin, X., and Zhang, L., 2019, Application of addition $HClO_4$ to improve the dissolution process and sensitivity of Os for low-concentration of Os in pyrite: Microchemical Journal, v. 150, article 104165, doi: 10.1016/j.microc.2019.104165.
Gao, R., Xue, C., Chi, G., Dai, J., Dong, C., Zhao, X., and Man, R., 2020, Genesis of the giant Caixiashan Zn-Pb deposit in Eastern Tianshan, NW China: Constraints from geology, geochronology and S-Pb isotopic geochemistry: Ore Geology Reviews, v. 119, article 103366, doi: 10.1016/j.oregeorev.2020.103366.
Garwin, S.L., 1997, The settings and styles of gold mineralization in Southeast Asia: Bulletin of the Geological Society of Malaysia, v. 40, p. 77–111.
Gunter, B., 2011, The exploration history, geology, and exploitation of the Buduk gold mine, West Kalimantan: An example of a small gold mine operation in Kalimantan: Majalah Geologi Indonesia, v. 26, p. 173–190.
Haile, N.S., 1973, West Borneo microplate younger than supposed?: Nature Physical Science, v. 242, p. 28–29, doi: 10.1038/physci242028a0.
Hall, R., 2012, Late Jurassic-Cenozoic reconstructions of the Indonesian region and the Indian ocean: Tectonophysics, v. 570–571, p. 1–41, doi: 10.1016/j.tecto.2012.04.021.
Hall, R., and Nichols, G., 2002, Cenozoic sedimentation and tectonics in Borneo: Climatic influences on orogenesis: Geological Society Special Publication, v. 191, p. 5–22, doi: 10.1144/GSL.SP.2002.191.01.02.
Hall, R., van Hattum, M.W.A., and Spakman, W., 2008, Impact of India-Asia collision on SE Asia: The record in Borneo: Tectonophysics, v. 451, p. 366–389.
Hansen, J., Skjerlie, K.P., Pedersen, R.B., and De La Rosa, J., 2002, Crustal melting in the lower parts of island arcs: An example from the Bremanger Granitoid Complex, west Norwegian Caledonides: Contributions to Mineralogy and Petrology, v. 143, p. 316–335, doi: 10.1007/s00410-001-0342-5.
Harahap, B.H., Abidin, H.Z., and Dahlius, A.Z., 2013, Metallogenic map of Indonesia, Bandung, Indonesia: Bandung, Indonesia, Geological Agency of Indonesia, scale 1:5,000,000.
Hassler, D.R., Peucker-Ehrenbrink, B., and Ravizza, G.E., 2000, Rapid determination of Os isotopic composition by sparging OsO_4 into a magnetic-sector ICP-MS: Chemical Geology, v. 166, p. 1–14, doi: 10.1016/S0009-2541(99)00180-1.
Hennig, J., Breitfeld, H.T., Hall, R., and Nugraha, A.M.S., 2017, The Mesozoic tectono-magmatic evolution at the Paleo-Pacific subduction zone in West Borneo: Gondwana Research, v. 48, p. 292–310, doi: 10.1016/j.gr.2017.05.001.
Hermanto, B., Bachri, S., and Atmawinata, S., 1994, Geological map of the Pankalanbuun quadrangle, Kalimantan, Bandung, Indonesia: Bandung, Indonesia, Geological Research and Development Centre, scale 1:250,000.
Hillier, S., and Velde, B., 1991, Octahedral occupancy and the chemical composition of diagenetic (low temperature) chlorites: Clay Mineralogy, v. 26, p. 149–168.
Hoefs, J., 2015, Stable isotope geochemistry: Berlin, Springer, 285 p., doi: 10.1007/978-3-662-02290-0.
Horie, K., Hidaka, H., and Gauthier-Lafaye, F., 2008, Elemental distribution in apatite, titanite and zircon during hydrothermal alteration: Durability of immobilization mineral phases for actinides: Physics and Chemistry of the Earth, Parts A/B/C, v. 33, p. 962–968, doi: 10.1016/j.pce.2008.05.008.
Horstwood, M.S.A., Košler, J., Gehrels, G., Jackson, S.E., McLean, N.M., Paton, C., Pearson, N.J., Sircombe, K., Sylvester, P., Vermeesch, P., Bowring, J.F., Condon, D.J., and Schoene, B., 2016, Community-derived standards for LA-ICP-MS U-(Th-)Pb geochronology: Uncertainty propagation, age interpretation and data reporting: Geostandards and Geoanalytical Research, v. 40, p. 311–332, doi: 10.1111/j.1751-908X.2016.00379.x.
Idrus, A., Setijadji, L.D., Tamba, F., and Anggara, F., 2011, Geology and characteristics of Pb-Zn-Cu-Ag skarn deposit at Ruwai, Lamandau Regency, Central Kalimantan: Journal of Applied Geology, v. 3, p. 191–201, doi: 10.22146/jag.7181.
Idrus, A., Dana, C.D.P., Lai, C.-K., Agangi, A., Takahashi, R., and Rajagukguk, E.H., 2023, Proximal to distal geochemical variations of the Ruwai polymetallic skarn deposit, Central Borneo, Indonesia: Insights from sulfides chemistry and implications to exploration: Journal of Geochemical Exploration, v. 246, article 107161, doi: 10.1016/j.gexplo.2023.107161.
Im, H., Jeong, J.-Y., and Shin, D., 2020, Genetic environment of W skarn and Pb-Zn vein mineralization associated with the Imog granite in the Taebaeksan mineralized district, South Korea: Ore Geology Reviews, v. 126, article 103721, doi: 10.1016/j.oregeorev.2020.103721.
Imai, A., 2000, Genesis of the Mamut porphyry copper deposit, Sabah, East Malaysia: Resource Geology, v. 50, p. 1–23, doi: 10.1111/j.1751-3928.2000.tb00052.x.
Jamtveit, B., Wogelius, R.A., and Fraser, D.G., 1993, Zonation patterns of skarn garnets: Records of hydrothermal system evolution: Geology, v. 21, p. 113–116, doi: 10.1130/0091-7613(1993)021<0113:ZPOSGR>2.3.CO;2.
Jansson, N.F., Allen, R.L., Skogsmo, G., and Turner, T., 2021, Origin of Palaeoproterozoic, sub-seafloor Zn-Pb-Ag skarn deposits, Sala area, Bergslagen, Sweden: Mineralium Deposita, v. 57, p. 455–480, doi: 10.1007/s00126-021-01071-2.
Kato, Y., Fujinaga, K., and Suzuki, K., 2005, Major and trace element geochemistry and Os isotopic composition of metalliferous umbers from the Late Cretaceous Japanese accretionary complex: Geochemistry, Geophysics, Geosystems, v. 6, article Q07004, doi: 10.1029/2005GC000920.
Keith, M., Haase, K.M., Schwarz-Schampera, U., Klemd, R., Petersen, S., and Bach, W., 2014, Effects of temperature, sulfur, and oxygen fugacity on the composition of sphalerite from submarine hydrothermal vents: Geology, v. 42, p. 699–702, doi: 10.1130/G35655.1.
Kimura, J.-I., Nozaki, T., Senda, R., and Suzuki, K., 2014, Precise determination of Os isotope ratios in the 15–4000 pg range using a sparging method using enhanced-sensitivity multiple Faraday collector-inductively coupled plasma-mass spectrometry: Journal of Analytical Atomic Spectrometry, v. 29, p. 1483–1490, doi: 10.1039/C4JA00092G.
Kostrovitsky, S.I., Skuzovatov, S.Y., Yakovlev, D.A., Sun, J., Nasdala, L., and Wu, F.-Y., 2016, Age of the Siberian craton crust beneath the northern kimberlite fields: Insights to the craton evolution: Gondwana Research, v. 39, p. 365–385, doi: 10.1016/j.gr.2016.01.008.
Kretschmar, U., and Scott, S.D., 1976, Phase relations involving arsenopyrite in the system Fe-As-S and their application: The Canadian Mineralogist, v. 14, p. 364–386.
Lai, C.-K., Xia, X.-P., Hall, R., Meffre, S., Tsikouras, B., Rosana Balangue-Tarriela, M.I., Idrus, A., Ifandi, E., and Norazme, N., 2021, Cenozoic evolution of the Sulu Sea arc-basin system: An overview: Tectonics, v. 40, article e2020TC006630, doi: 10.1029/2020TC006630.
Li, S., Yang, X., and Sun, W., 2015, The Lamandau IOCG deposit, southwestern Kalimantan Island, Indonesia: Evidence for its formation from geochronology, mineralogy, and petrogenesis of igneous host rocks: Ore Geology Reviews, v. 68, p. 43–58, doi: 10.1016/j.oregeorev.2015.01.008.
Li, S., Sun, S., Yang, X., Sun, W., and Wu, Z., 2021, Detrital zircon U-Pb age perspective on the sediment provenance and its geological significance of sandstones in the Lamandau region, SW Borneo, Indonesia: Journal of Oceanology and Limnology, v. 40, p. 496–514, doi: 10.1007/s00343-021-0405-6.
Li, X.H., Long, W.G., Li, Q.L., Liu, Y., Zheng, Y.F., Yang, W.H., Chamberlain, K.R., Wan, D.F., Guo, C.H., Wang, X.C., and Tao, H., 2010, Penglai zircon megacrysts: A potential new working reference material for microbeam determination of Hf-O isotopes and U-Pb age: Geostandards and Geoanalytical Research, v. 34, p. 117–134, doi: 10.1111/j.1751-908X.2010.00036.x.
Lin, J., Liu, Y., Yang, Y., and Hu, Z., 2016, Calibration and correction of LA-ICP-MS and LA-MC-ICP-MS analyses for element contents and isotopic ratios: Solid Earth Sciences, v. 1, p. 5–27, doi: 10.1016/j.sesci.2016.04.002.
Luck, J.M., and Allegre, C.J., 1983, ^{187}Re-^{187}Os systematics in meteorites and cosmochemical consequences: Nature, v. 302, p. 130–132, doi: 10.1038/302130a0.
Maniar, P.D., and Piccoli, P.M., 1989, Tectonic discrimination of granitoids: Geological Society of America Bulletin, v. 101, p. 635–643.
Margono, U., Soejitno, T., and Santosa, T., 1995, Geological map of the Tumbangmanjul Quadrangle, Kalimantan, Bandung, Indonesia: Bandung,

Indonesia, Geological Research and Development Centre of Indonesia, scale 1:250,000.
McDonough, W.F., and Sun, S.-S., 1995, The composition of the Earth: Chemical Geology, v. 120, p. 223–253, doi: 10.1016/0009-2541(94)00140-4.
Megaw, P.K.M., Ruiz, J., and Titley, S.R., 1988, High-temperature, carbonate-hosted Ag-Pb-Zn(Cu) deposits of northern Mexico: Economic Geology, v. 83, p. 1856–1885, doi: 10.2113/gsecongeo.83.8.1856.
Meinert, L.D., 1992, Skarn and skarn deposits: Geoscience Canada, v. 19, p. 145–162, doi: 0.12789/gs.v19i4.3773.
Meinert, L.D., Hedenquist, J.W., Satoh, H., and Matsuhisa, Y., 2003, Formation of anhydrous and hydrous skarn in Cu-Au ore deposits by magmatic fluids: Economic Geology, v. 98, p. 147–156, doi: 10.2113/gsecongeo.98.1.147.
Meinert, L.D., Dipple, G.M., and Nicolescu, S., 2005, World skarn deposits: Economic Geology 100th Anniversary Volume, p. 299–336, doi: 10.5382/av100.11.
Metcalfe, I., 2013, Gondwana dispersion and Asian accretion: Tectonic and palaeogeographic evolution of eastern Tethys: Journal of Asian Earth Sciences, v. 66, p. 1–33, doi: 10.1016/j.jseaes.2012.12.020.
Morgan, J.W., Golightly, D.W., and Dorrzapf, A.F., 1991, Methods for the separation of rhenium, osmium and molybdenum applicable to isotope geochemistry: Talanta, v. 38, p. 259–265, doi: 10.1016/0039-9140(91)80045-2.
Morley, R.J., 1998, Palynological evidence for Tertiary plant dispersals in the SE Asian region in relation to plate tectonics and climate: Biogeography and Geological Evolution of SE Asia, v. 1, p. 211–234.
Norman, M., Bennett, V., McCulloch, M., and Kinsley, L., 2002, Osmium isotopic compositions by vapor phase sample introduction using a multicollector ICP-MS: Journal of Analytical Atomic Spectrometry, v. 17, p. 1394–1397, doi: 10.1039/b204518d.
Nozaki, T., Suzuki, K., Ravizza, G., Kimura, J.-I., and Chang, Q., 2012, A method for rapid determination of Re and Os isotope compositions using ID-MC-ICP-MS combined with the sparging method: Geostandards and Geoanalytical Research, v. 36, p. 131–148, doi: 10.1111/j.1751-908X.2011.00125.x.
Ohmoto, H., and Rye, R.O., 1979, Isotopes of sulphur and carbon, *in* Barnes, H.L., ed., Geochemistry of hydrothermal ore deposits, 2nd ed.: New York, Wiley, p. 509–567.
Ohta, J., Nozaki, T., Sato, H., Ashida, K., and Kato, Y., 2022, Precise and accurate analytical method for determination of osmium isotope ratios at the 1–15 pg level by MC-ICP-MS equipped with sparging introduction and high-sensitivity discrete dynode-type ion-counting detectors: Journal of Analytical Atomic Spectrometry, v. 37, p. 1600–1610, doi: 10.1039/D2JA00089J.
O'Neill, J.R., and Taylor, H.P., Jr., 1967, The oxygen isotope and cation exchange chemistry of feldspars: American Mineralogist, v. 52, p. 1414–1437.
Palinkaš, S.S., Palinkaš, L.A., Renac, C., Spangenberg, J.E., Lüders, V., Molnar, F., and Maliqi, G., 2013, Metallogenic model of the Trepča Pb-Zn-Ag skarn deposit, Kosovo: Evidence from fluid inclusions, rare earth elements, and stable isotope data: Economic Geology, v. 108, p. 135–162, doi: 10.2113/econgeo.108.1.135.
Paton, C., Hellstrom, J., Paul, B., Woodhead, J., and Hergt, J., 2011, Iolite: Freeware for the visualisation and processing of mass spectrometric data: Journal of Analytical Atomic Spectrometry, v. 26, p. 2508–2518, doi: 10.1039/c1ja10172b.
Pearce, J.A., 1996, A user's guide to basalt discrimination diagrams: Geological Association of Canada Short Course Notes, v. 12, p. 79–113.
Pearce, J.A., Harris, N.B., and Tindle, A.G., 1984, Trace element discrimination diagrams for the tectonic interpretation of granitic rocks: Journal of Petrology, v. 25, p. 956–983.
Percival, T.J., Hofstra, A.H., Gibson, P.C., Noble, D.C., Radtke, A.S., Bagby, W.C., Pickthorn, W.J., and McKee, E.H., 2018, Sedimentary rock-hosted gold deposits related to epizonal intrusions, Bau district, Island of Borneo, Sarawak, East Malaysia: Reviews in Economic Geology, v. 20, p. 259–297, doi: 10.5382/rev.20.08.
Petrus, J.A., and Kamber, B.S., 2012, VizualAge: A novel approach to laser ablation ICP-MS U-Pb geochronology data reduction: Geostandards and Geoanalytical Research, v. 36, p. 247–270.
Peucker-Ehrenbrink, B., and Jahn, B., 2001, Rhenium-osmium isotope systematics and platinum group element concentrations: Loess and the upper continental crust: Geochemistry, Geophysics, Geosystems, v. 2, p. 1–22, doi: 10.1029/2001GC000172.
Powell, R., 1985, Regression diagnostics and robust regression in geothermometer/geobarometer calibration: The garnet-clinopyroxene geothermometer revisited: Journal of Metamorphic Geology, v. 3, p. 231–243.
Schoenberg, R., Nägler, T.F., and Kramers, J.D., 2000, Precise Os isotope ratio and Re-Os isotope dilution measurements down to the picogram level using multicollector inductively coupled plasma mass spectrometry: International Journal of Mass Spectrometry, v. 197, p. 85–94, doi: 10.1016/S1387-3806(99)00215-8.
Seal, R.R., II, 2006, Sulfur isotope geochemistry of sulfide minerals: Reviews in Mineralogy and Geochemistry, v. 61, p. 633–677, doi: 10.2138/rmg.2006.61.12.
Segal, I., Halicz, L., and Platzner, I.T., 2003, Accurate isotope ratio measurements of ytterbium by multiple collection inductively coupled plasma mass spectrometry applying erbium and hafnium in an improved double external normalization procedure: Journal of Analytical Atomic Spectrometry, v. 18, p. 1217–1223, doi: 10.1039/B307016F.
Seman, S., Stockli, D.F., and McLean, N.M., 2017, U-Pb geochronology of grossular-andradite garnet: Chemical Geology, v. 460, p. 106–116, doi: 10.1016/j.chemgeo.2017.04.020.
Setiabudi, B.T., 2001, Geochemistry and geochronology of the igneous suite associated with the Kelian epithermal gold deposit, Indonesia: Unpublished Ph.D. thesis, Canberra, Australia, Australian National University, 132 p.
Setiawan, N.I., Osanai, Y., Nakano, N., Adachi, T., Setiadji, L.D., and Wahyudiono, J., 2013, Late Triassic metatonalite from the Schwaner Mountains in West Kalimantan and its contribution to sedimentary provenance in the Sundaland: Berita Sedimentologi, v. 28, p. 4–12.
Setijadji, L.D., Basuki, N.I., and Prihatmoko, S., 2010, Kalimantan mineral resources: An update on exploration and mining trends, synthesis on magmatism history and proposed models for metallic mineralization: Ikatan Ahli Geologi Indonesia (IAGI; Indonesian Association of Geologists) Annual Convention, 39th, Lombok, Indonesia, November 22–25, 2010, Proceedings, p. 14–28.
Setijadji, L.D., Tamba, F., and Idrus, A., 2011, Geology of the Ruwai iron and Zn-Pb-Ag skarn deposits Lamandau district, Central Kalimantan: Majalah Geologi Indonesia, v. 26, p. 143–154.
Shimazaki, H., and Kusakabe, M., 1990, Oxygen isotope study of the Kamioka Zn-Pb skarn deposits, central Japan: Mineralium Deposita, v. 25, p. 221–229, doi: 10.1007/BF00190385.
Shirey, S.B., and Walker, R.J., 1995, Carius tube digestion for low-blank rhenium-osmium analysis: Analytical Chemistry, v. 67, p. 2136–2141, doi: 10.1021/ac00109a036.
——1998, The Re-Os isotope system in cosmochemistry and high-temperature geochemistry: Annual Review of Earth and Planetary Science, v. 26, p. 423–500.
Simbolon, D., Dana, C.D.P., and Whitehouse, L., 2019, Metallogenic model of the Ruwai Fe-Zn-Pb-Ag skarn deposit, Central Borneo: Understanding the complexity from proximal to distal basemetal mineralization: Masyarakat Geologi Ekonomi Indonesia (MGEI; Indonesian Society of Economic Geologists), 11th, Unlocking Concealed and Complex Deposits, Bogor, Indonesia, September 24–26, 2019, Proceedings, p. 115–122.
Sláma, J., Košler, J., Condon, D.J., Crowley, J.L., Gerdes, A., Hanchar, J.M., Horstwood, M.S.A., Morris, G.A., Nasdala, L., Norberg, N., Schaltegger, U., Schoene, B., Tubrett, M.N., and Whitehouse, M.J., 2008, Plešovice zircon: A new natural reference material for U-Pb and Hf isotopic microanalysis: Chemical Geology, v. 249, p. 1–35, doi: 10.1016/j.chemgeo.2007.11.005.
Smith, M.P., Henderson, P., Jeffries, T.E.R., Long, J., and Williams, C.T., 2004, The rare earth elements and uranium in garnets from the Beinn an Dubhaich Aureole, Skye, Scotland, UK: Constraints on processes in a dynamic hydrothermal system: Journal of Petrology, v. 45, p. 457–484, doi: 10.1093/petrology/egg087.
Soeria-Atmadja, R., Noeradi, D., and Priadi, B., 1999, Cenozoic magmatism in Kalimantan and its related geodynamic evolution: Journal of Asian Earth Sciences, v. 17, p. 25–45, doi: 10.1016/S0743-9547(98)00062-2.
Song, S., Mao, J., Xie, G., Chen, L., Santosh, M., Chen, G., Rao, J., and Ouyang, Y., 2019, In situ LA-ICP-MS U-Pb geochronology and trace element analysis of hydrothermal titanite from the giant Zhuxi W (Cu) skarn deposit South China: Mineralium Deposita, v. 54, p. 569–590, doi: 10.1007/s00126-018-0831-3.
Spandler, C., Hammerli, J., Sha, P., Hilbert-Wolf, H., Hu, Y., Roberts, E., and Schmitz, M., 2016, MKED1: A new titanite standard for in situ analysis of Sm-Nd isotopes and U-Pb geochronology: Chemical Geology, v. 425, p. 110–126, doi: 10.1016/j.chemgeo.2016.01.002.

Stein, H.J., Morgan, J.W., and Schersten, A., 2000, Re-Os dating of low-level highly radiogenic (LLHR) sulfides: The Harnäs gold deposit, southwest Sweden, records continental-scale tectonic events: Economic Geology, v. 95, p. 1657–1671, doi: 10.2113/gsecongeo.95.8.1657.

Sun, S.-S., and McDonough, W.F., 1989, Chemical and isotopic systematics of oceanic basalts: Implications for mantle composition and processes: Geological Society, London, Special Publications, v. 42, p. 313–345, doi: 10.1144/GSL.SP.1989.042.01.19.

Thompson, J.F.H., Abidin, H.Z., Both, R.A., Martosuroyo, S., Rafferty, W.J., and Thompson, A.J.B., 1994, Alteration and epithermal mineralization in the Masupa Ria volcanic center, Central Kalimantan, Indonesia: Journal of Geochemical Exploration, v. 50, p. 429–456, doi: 10.1016/0375-6742(94)90035-3.

Tsikouras, B., Lai, C.-K., Ifandi, E., Norazme, N.A., Teo, C.-H., and Xia, X.-P., 2021, New zircon radiometric U-Pb ages and Lu-Hf isotopic data from the ultramafic-mafic sequences of Ranau and Telupid (Sabah, eastern Malaysia): Time to reconsider the geological evolution of Southeast Asia?: Geology, v. 49, p. 789–793, doi: 10.1130/G48126.1.

van Bemmelen, R.W., 1949, The geology of Indonesia: Amsterdam, The Hague, 265 p.

van Leeuwen, T.M., 2018, Twenty five more years of mineral exploration in Indonesia (1993–2017): Masyarakat Geologi Ekonomi Indonesia 10th Anniversary Special Publication, 318 p.

van Leeuwen, T.M., Leach, T.M., Hawke, A.A., and Hawke, M.M., 1990, The Kelian disseminated gold deposit, East Kalimantan, Indonesia: Journal of Geochemical Exploration, v. 35, p. 1–61, doi: 10.1016/0375-6742(90)90035-9.

Vazquez, R., Vennemann, T.W., Kesler, S.E., and Russell, N., 1998, Carbon and oxygen isotope halos in the host limestone, El Mochito Zn-Pb-(Ag) skarn massive sulfide-oxide deposit, Honduras: Economic Geology, v. 93, p. 15–31, doi: 10.2113/gsecongeo.93.1.15.

Vermeesch, P., 2018, IsoplotR: A free and open toolbox for geochronology: Geoscience Frontiers, v. 9, p. 1479–1493, doi: 10.1016/j.gsf.2018.04.001.

Wafforn, S., Seman, S., Kyle, J.R., Stockli, D., Leys, C., Sonbait, D., and Cloos, M., 2018, Andradite garnet U-Pb geochronology of the Big Gossan skarn, Ertsberg-Grasberg mining district, Indonesia: Economic Geology, v. 113, p. 769–778, doi: 10.5382/econgeo.2018.4569.

Wang, Y., Liu, Z., Murtadha, S., Cawood, P.A., Qian, X., Ghani, A., Gan, C., Zhang, Y., Wang, Y., Li, S., and Zhang, P., 2022a, Jurassic subduction of the Paleo-Pacific plate in Southeast Asia: New insights from the igneous and sedimentary rocks in West Borneo: Journal of Asian Earth Sciences, v. 232, article 105111, doi: 10.1016/j.jseaes.2022.105111.

Wang, Y., Wu, S., Qian, X., Cawood, P.A., Lu, X., Gan, C., Asis, J.B., and Zhang, P., 2022b, Early Cretaceous subduction in NW Kalimantan: Geochronological and geochemical constraints from the Raya and Mensibau igneous rocks: Gondwana Research, v. 101, p. 243–256, doi: 10.1016/j.gr.2021.08.006.

Widyastanto, A., Brojomusti, J., Dana, C.D.P., Fatratomo, F., and Santayana, H., 2019, Mineralogical characteristics of granitoid and mafic intrusive bodies in Ruwai skarn Zn-Pb-Ag deposit: A preliminary study on pre to post mineralization intrusion: , Himpunan Ahli Geofisika Indonesia (Indonesian Association of Geophysicists)-Ikatan Ahli Geologi Indonesia (Indonesian Association of Geologists)-Ikatan Ahli Fasilitas Produksi Minyak dan Gas Bumi Indonesia (Indonesian Association of Production Facilities for Oil and Gas)-Ikatan Ahli Teknik Perminyakan Indonesia (Indonesian Association of Petroleum Engineers) (HAGI-IAGI-IAFMI-IATMI) Joint Convention, Yogyakarta, Indonesia, November 25–29, 2019, Proceedings, p. 1–8.

Wiedenbeck, M., Allé, P., Corfu, F., Griffin, W.L., Meier, M., Oberli, F., von Quadt, A., Roddick, J.C., and Spiegel, W., 1995, Three natural zircon standards for U-Th-Pb, Lu-Hf, trace element and REE analyses: Geostandards Newsletter, v. 19, p. 1–23, doi: 10.1111/j.1751-908X.1995.tb00147.x.

Williams, P.R., and Harahap, B.H., 1987, Preliminary geochemical and age data from postsubduction intrusive rocks, northwest Borneo: Australian Journal of Earth Sciences, v. 34, p. 405–415, doi: 10.1080/08120098708729422.

Williams, P.R., Johnston, C.R., Almond, R.A., and Simamora, W.H., 1988, Late Cretaceous to early Tertiary structural elements of West Kalimantan: Tectonophysics, v. 148, p. 279–297, doi: 10.1016/0040-1951(88)90135-7.

Wilson, A.J., Cooke, D.R., Harper, B.J., and Deyell, C.L., 2007, Sulfur isotopic zonation in the Cadia district, southeastern Australia: Exploration significance and implications for the genesis of alkalic porphyry gold-copper deposits: Mineralium Deposita, v. 42, p. 465–487, doi: 10.1007/s00126-006-0071-9.

Xu, J., Xia, X.P., Lai, C.K., Long, X., and Huang, C., 2019, When did the Paleotethys Ailaoshan Ocean close: New insights from detrital zircon U-Pb age and Hf isotopes: Tectonics, v. 38, p. 1798–1823, doi: 10.1029/2018TC005291.

Yanagisawa, F., and Sakai, H., 1983, Thermal decomposition of barium sulfate vanadium pentaoxide-silica glass mixtures for preparation of sulfur dioxide in sulfur isotope ratio measurements: Analytical Chemistry, v. 55, p. 985–987.

Zane, A., and Weiss, Z., 1998, A procedure for classifying rock-forming chlorites based on microprobe data: Rendiconti Lincei, v. 9, p. 51–56, doi: 10.1007/BF02904455.

Zhong, S., Feng, C., Seltmann, R., Li, D., and Dai, Z., 2018, Geochemical contrasts between Late Triassic ore-bearing and barren intrusions in the Weibao Cu-Pb-Zn deposit, East Kunlun Mountains, NW China: Constraints from accessory minerals (zircon and apatite): Mineralium Deposita, v. 53, p. 855–870, doi: 10.1007/s00126-017-0787-8.

Zhu, J., Li, S., and Murtadha, S., 2022, Oldest (ca. 462 Ma) basement in Indonesian Borneo and its implication for the early Paleozoic tectonic evolution of Southeast Asia: Acta Geologica Sinica, v. 96, p. 1–15, doi: 10.1111/1755-6724.14956.

Cendi D.P. Dana is currently a full-time Ph.D. student at the School of GeoSciences, The University of Edinburgh, establishing geochemical vectors to aid the discovery of metamorphosed volcanogenic massive sulfide deposits, particularly in Archean terranes. He earned his M.Sc. degree in earth resource science at Akita University, Japan, where he elucidated the base metal mineralization in the Central Borneo metallogenic belt. He also holds a B.Eng. degree in geological engineering from Universitas Gadjah Mada, Indonesia, where he investigated the geology of epithermal gold-base metal deposits in Western Java. Prior his master's study, he worked at PT Kapuas Prima Coal, Tbk., as a brownfield exploration geologist looking for skarn deposits within the Schwaner Mountains, Central Borneo. He also joined a summer internship program with Japan Gold Corp. during his master's study for a soil sampling campaign associated with the Ikutahara epithermal gold project at Hokkaido.